doses of effective H5N1 vaccine, the seed viruses are required to have high-level growth properties. Currently, prepandemic H5N1 vaccines, including the NIBRG-14-based vaccine recommended by the World Health Organization (WHO), are being stockpiled (2). These viruses comprise an HA gene whose cleavage site has been modified to an avirulent type (the mHA gene) and a neuraminidase (NA) gene, both derived from an H5N1 strain, and six remaining genes, derived from a high-growing donor virus (creating a so-called 6:2 reassortant). The WHO recommends A/Puerto Rico/8/34 (H1N1; PR8) as a donor strain for vaccine seed viruses because of its safety in humans and its high-level growth property in eggs (34). Previously, we found that the growth property of vaccine seed viruses in eggs depends on the genes encoding the internal proteins of the donor virus (10). Therefore, with respect to H5N1 vaccine production in MDCK cells, it is necessary to select a high-growth donor strain, whose internal proteins function efficiently in this cell line.

In this study, we found that the H5N1 6:2 reassortant viruses with our laboratory strain of PR8 [PR8(UW)] (10) as the background grew significantly better than NIBRG-14 with the PR8(Cambridge) background in MDCK cells. We therefore sought to determine the molecular basis of this difference in growth, which would contribute to the robustness of MDCK cell-based H5N1 vaccines, and tested whether the HA/NA functional balance regulates the growth of the vaccine seed viruses in MDCK cells, as it does in eggs (10). Our results should help to establish MDCK cell-based H5N1 vaccine production as a viable option for large-scale vaccine production in the event of a pandemic.

MATERIALS AND METHODS

Cells. MDCK cells, maintained in our laboratory, were grown in minimal essential medium (MEM) with 5% newborn calf serum. 293T human embryonic kidney cells were maintained in Dulbecco's modified Eagle's MEM with 10% fetal calf serum. A72 canine tumor fibroblasts (13) were maintained in L15 medium (GIBCO-BRL) with 20% fetal calf serum. Cells were maintained at 37°C in 5% CO_2.

Viruses. The H5N1 A/Vietnam/UT30259/04 (VN30259), A/Vietnam/UT3030/04 (VN3030), A/Indonesia/UT3006/05 (Indo3006), and A/Anhui/2/05 (AH2) strains were propagated in 10-day-old embryonated chicken eggs at 37°C for 48 h, after which time the allantoic fluids containing viruses were harvested. All experiments with these infectious viruses were carried out in a biosafety level 3 containment laboratory. The WHO-recommended vaccine seed virus, NIBRG-14 (PR8/VN1194 6:2 reassortant), was a kind gift from J. Wood and J. Robertson at the National Institute for Biological Standards and Control, United Kingdom. Recombinant vesicular stomatitis virus (VSV) carrying the green fluorescent protein (GFP) gene instead of the G protein gene (VSV-ΔG*-GFP) (30) was kindly provided by M. A. Whitt at the University of Tennessee, Memphis, TN.

Construction of plasmids and reverse genetics. To generate reassortants of influenza A viruses, we used plasmid-based reverse genetics (23). Viral RNA was extracted from the allantoic fluids by using a commercial kit (ISOGEN LS; Nippon Gene) and was converted to cDNA by using reverse transcriptase (SuperScript III; GIBCO-BRL) and primers containing the consensus sequences of the 3-prime ends of the RNA segments for the H5 viruses. The full-length cDNAs were then PCR amplified with ProofStart polymerase (Qiagen) and with segment-specific primer pairs and cloned into a plasmid under the control of the human polymerase I (PolI) promoter and the mouse RNA PolI terminator (PolI plasmids). By inverse PCR using back-to-back primer pairs followed by ligation, we altered the HA gene sequence that encodes the cleavage site of the wild-type VN30259, VN3030, Indo3006 (RERRRKKR), and AH2 (RERRRKR) viruses to create the avirulent-type sequence (RETR), as described elsewhere (11). We also constructed PolI-VN30259NA, PolI-VN3030NA, PolI-Indo3006NA, and pPolI-AH2NA plasmids containing the NA genes by using reverse transcription-PCR with N1-specific primers. We additionally constructed pPolI-VN1203FillNA with the insertion of a 20-amino-acid-encoding sequence derived from the A/goose/Guandong/1/96 NA stalk region into VN1203NA (VN1203FillNA). All of these constructs were sequenced to verify the absence of unwanted mutations. Primer sequences will be provided upon request.

We used our previously produced series of PolI constructs, derived from the PR8(UW) and PR8(Cambridge) strains, for reverse genetics (10, 11) and also used PolI plasmids containing mHA genes derived from VN1194 and VN1203 and NA genes derived from A/WSN/33 (H1N1; WSN), A/Hong Kong/213/03 (H5N1; HK213), and A/Kanagawa/173/2001 (H1N1; Kanagawa) (11, 17, 23).

Chimeric PB2 genes were constructed by switching the fragments at two BsmBI sites between pPolI-PR8(UW)PB2 and pPolI-PR8(Cambridge)PB2. To generate PB2 and NS mutants, PolI plasmids expressing the PB2 and NS genes of PR8 were used as templates for site-directed mutagenesis by the inverse PCR method. Plasmids expressing PR8 NP, PA, PB1, or PB2 under the control of the chicken β-actin promoter were used for all reverse genetics experiments. Briefly, PolI plasmids and protein expression plasmids were mixed with a transfection reagent, Trans-IT 293T (Panvera); incubated at room temperature for 15 min; and then added to 293T cells. Transfected cells were incubated in Opti-MEM I (GIBCO-BRL) for 48 h. Supernatants containing infectious viruses were harvested and propagated in 10-day-old embryonated chicken eggs at 37°C for 48 h, after which time the allantoic fluids containing virus were harvested and stored at −80°C until use.

Viral replication in MDCK cells. Virus was inoculated into MDCK cell monolayers at a multiplicity of infection (MOI) of 0.01 PFU with MEM containing 0.3% bovine serum albumin and 0.8 μg/ml TPCK-trypsin and incubated at 33°C. Viruses in the culture supernatants were collected at a given number of hours postinfection (hpi) and then titrated by use of an MDCK plaque assay to determine the virus titers. The plaque sizes (at least 15 plaques for each virus) were measured by micrometer calipers after staining with crystal violet.

Luciferase assay-based assessment of viral polymerase activity. The viral polymerase activity was measured as described previously (24). All experiments were independently performed in triplicate. Briefly, pPolIC250-NP(0)Fluc(0), a luciferase reporter plasmid under the control of the canine PolI promoter (22), was cotransfected into MDCK cells by using plasmids expressing PR8(UW) PB1, PA, and NP and either PB2 derived from PR8(UW) or PR8(Cambridge) or mutant PB2 under the control of the chicken β-actin promoter. The cells were subjected to a dual-luciferase reporter assay system (Promega, Madison, WI) on a microplate luminometer (Veritas; Turner Biosystems, Sunnyvale, CA) according to the manufacturer's instructions. pGL4.74[hRluc/TK] (Promega) was used as an internal control.

IFN bioassay. Levels of interferon (IFN) secreted by virus-infected canine cells were determined as previously described (13, 25), with some modifications. Briefly, MDCK cells were infected with wild-type or NS1 mutant viruses at an MOI of 2. Supernatants from infected cells were harvested 24 hpi and then treated with UV light for 20 min to inactivate the infectivity of the virus. UV-treated supernatants were then added to A72 cells and incubated for 20 h before being infected with VSV-ΔG*-GFP at an MOI of 1. Adherent cells were detached by vigorous pipetting in phosphate-buffered saline at 12 hpi and then washed once with cold phosphate-buffered saline supplemented with 2% fetal calf serum and 0.1% sodium azide (wash buffer). Cells were washed again before the number of cells expressing GFP was counted by FACSCalibur with Cell Quest software (Becton Dickinson).

Statistical analysis. All comparisons of the infectivity titers, relative luciferase activities, numbers of GFP-positive cells, and plaque diameters of each virus relied on Student's *t* test with two-tailed analysis to determine significant differences.

RESULTS

Growth of PR8/VN1194 6:2 reassortant viruses in MDCK cells. To assess the replication abilities of two PR8/VN1194 6:2 reassortants, PR8(UW)/VN1194H5N1 [PR8(UW) strain background] and NIBRG-14 [PR8(Cambridge) strain background], in MDCK cells, we examined the plaque-forming characteristics of these viruses and their growth kinetics. PR8(UW)/VN1194H5N1 formed larger plaques (Fig. 1A) and grew significantly better than NIBRG-14 (Fig. 1B). The peak viral titer reached $3.2 \times 10^7 \pm 1.2 \times 10^7$ PFU/ml at 36 hpi for PR8(UW)/VN1194H5N1, compared to $6.8 \times 10^4 \pm 1.5 \times 10^4$ PFU/ml at

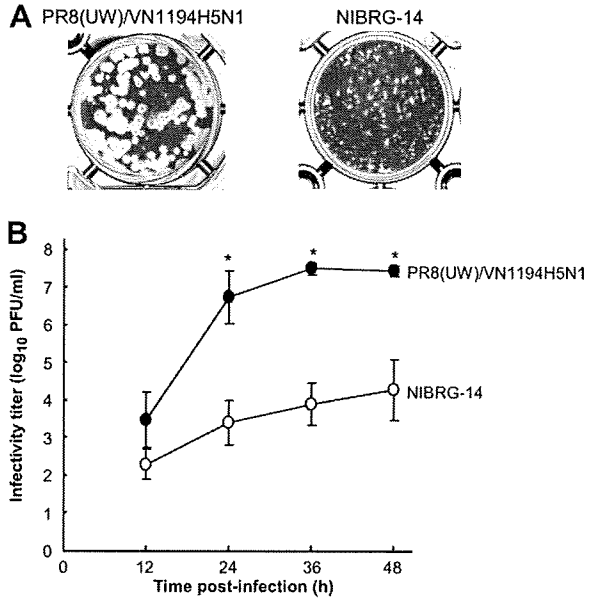

FIG. 1. Growth of PR8/H5N1 6:2 reassortant viruses in MDCK cells. (A) Plaque morphology of PR8(UW)/VN1194H5N1 and WHO-recommended NIBRG-14 on MDCK cells. (B) Viral titers of PR8(UW)/VN1194H5N1 and NIBRG-14 were determined at 12, 24, 36, and 48 hpi at an MOI of 0.01. The data are reported as mean titers with standard deviations for three independent experiments. Virus titers with significant growth enhancement relative to those of NIBRG-14 ($P < 0.05$; Student t test with two-tail analysis) are shown (*).

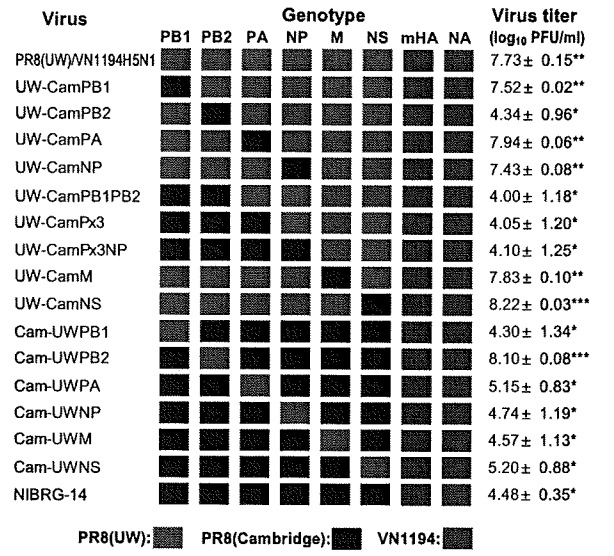

FIG. 2. Growth of PR8/H5N1 reassortant viruses in MDCK cells. All viruses possess mHA and NA, both derived from VN1194 (green), and their remaining genes are from either PR8(UW) (red) or PR8(Cambridge) (blue). Cells were infected with each virus at an MOI of 0.01. Virus titers were determined in a plaque assay with MDCK cells at 36 hpi. The data are shown as mean titers with standard deviations ($n \geq 3$). Titers significantly ($P < 0.05$) decreased (*) or increased (***) compared with that of PR8(UW)/VN1194H5N1 are shown. Titers significantly increased (**) compared with that of NIBRG-14 are also shown.

48 hpi for NIBRG-14. These two viruses have identical HAs and NAs, indicating that our PR8(UW) strain is responsible for the superior growth kinetics relative to those for the PR8(Cambridge) strain background of H5N1 vaccine seed virus in MDCK cells.

Growth of reassortants between the PR8(UW) and PR8(Cambridge) strains. To identify the genes responsible for the superior growth of our 6:2 reassortant, we made a series of gene reassortants between the PR8(UW) and PR8(Cambridge) strains with VN1194 mHA and NA and measured their viral titers in MDCK cells (Fig. 2). Every reassortant possessing PR8(Cambridge) PB2 exhibited significantly poorer growth (more than 3 logs lower) than PR8(UW)/VN1194H5N1 ($P < 0.01$; Student's t test). Conversely, the reassortant Cam-UWPB2 virus that possesses PR8(UW) PB2 with PR8(Cambridge) as the background grew significantly better than NIBRG-14 ($P < 0.01$). These results indicated that PR8(UW) PB2 is responsible for the high growth of PR8(UW)/VN1194H5N1 in MDCK cells.

Interestingly, the reassortant UW-CamNS virus that possesses the PR8(Cambridge) NS gene with the PR8(UW) background grew significantly better than PR8(UW)/VN1194H5N1 ($P < 0.01$). This result indicates that the PR8(Cambridge) NS gene product enhanced viral growth in MDCK cells, although a negative effect was not observed when the NS gene of NIBRG-14 was replaced with that of the PR8(UW) (i.e., Cam-UWNS) strain.

These observations demonstrate that it is PB2 that primarily is responsible for the difference in virus growth in MDCK cells between PR8(UW)/VN1194H5N1 and NIBRG-14 but that NS also partially contributes to this difference.

PB2 is responsible for viral growth in MDCK cells. To determine the amino acid residues that determine virus growth in MDCK cells, we compared the PB2 amino acid sequence of PR8(UW) with that of PR8(Cambridge) and found six amino acid differences between the two strains (Table 1). To identify which residue(s) is responsible for virus growth, we generated two PB2 chimeric viruses whose other internal genes came from PR8(UW); chimera 1 possesses the amino-terminal portion (residues 1 to 387) of PR8(Cambridge) PB2 and the carboxyl-terminal portion (residues 388 to 759) of PR8(UW) PB2, and chimera 2 possesses the opposite configuration. When we tested the viral titers of chimeras 1 and 2 in MDCK cells, the titers were found to be 5.0×10^3 PFU/ml and 3.9×10^7 PFU/ml, respectively (Fig. 3A), revealing that the amino acid difference(s) in the amino-terminal portion is responsible for virus growth in MDCK cells. Therefore, we made an additional four PB2 mutant viruses with single-amino-acid substitutions at positions 105, 251, 299, and 360 of PR8(UW) PB2 and assessed the titer of each virus (Fig. 3A). Among these viruses, UW-Y360SUWPB2, which contains a Tyr-to-Ser substitution at position 360 of PB2, grew poorly, with a titer of 1.5×10^3 PFU/ml, which was approximately 1,000 times lower than that of PR8(UW)/VN1194H5N1. Notably, this titer was significantly lower than that of NIBRG-14 ($P < 0.05$). Conversely, an NIBRG-14 mutant with a single-amino-acid substitution of Ser to Tyr at position 360 of Cambridge PB2 (NIB-S360YCamPB2) showed a viral titer comparable to that of PR8(UW)/VN1194H5N1. These results demonstrated that Tyr

TABLE 1. Amino acid differences between the PR8 strains for proteins other than HA and NA

Protein	Position	Amino acid for indicated strain	
		PR8(Cambridge)	PR8(UW)
PA	158	R	K
	550	L	I
PB1	175	K	N
	205	I	M
	208	R	K
	216	G	S
	563	R	I
PB1-F2	59	K	R
	60	Q	R
PB2	105	M	I
	251	K	R
	299	K	R
	360	S	Y
	504	V	I
	702	R	K
NP	353	V	L
	425	V	I
	430	T	N
M2	27	A	T
	39	I	T
NS1	55	E	K
	101	E	D
NS2	89	V	I

at position 360 of PR8(UW) PB2 gives rise to the high efficiency of viral growth in MDCK cells.

To address the molecular basis for the importance of the amino acid at position 360 of PB2, we assessed the polymerase activity of the viral polymerase complex containing each PB2 in MDCK cells by using a polymerase activity assay with luciferase as a reporter (24). For this assay, plasmids expressing either PB2 of PR8(UW), PR8(Cambridge), or their mutants were cotransfected into MDCK cells by using four plasmids expressing PR8(UW) PB1, PA, and NP and a reporter plasmid expressing luciferase under the control of the canine PolI promoter (22). At 24 h posttransfection, the cells were lysed and the luciferase activity of the lysates was measured as an indicator of viral polymerase activity (Fig. 3B). The cell lysates transfected with the plasmid expressing PR8(UW) PB2 or PR8(Cambridge) S360Y mutant PB2 exhibited significantly higher luciferase activities than those of PR8(Cambridge) PB2 and PR8(UW) Y360S mutant PB2. These data indicate that the amino acid at position 360 of PB2 is responsible for viral polymerase activity in MDCK cells and is likely the impetus for the different growth rates among viruses.

The role of NS for viral growth in MDCK cells. To address the role of NS for virus growth in MDCK cells, we compared the NS amino acid sequences of PR8(UW) and PR8(Cambridge) and found two amino acid differences in NS1 and one difference in NS2 between the two strains (Table 1). To determine which residue(s) is involved in viral growth kinetics, we generated NS1 mutant viruses with a single-amino-acid substitution either at position 55 or at position 101 of NS1 and assessed each viral titer (Fig. 4A). When a Lys-to-Glu substitution at position 55 was introduced into NS1 of PR8(UW)/VN1194H5N1 (UW-K55EUWNS1), the virus grew significantly better than its parent, PR8(UW)/VN1194H5N1 ($P < 0.05$). However, when a Glu-to-Lys substitution at the same position was introduced into PR8(Cambridge) NS1 of a PR8(UW)/VN1194H5N1-based mutant, UW-CamNS (see Fig. 2 for gene constellation) (UW-E55KCamNS1), the virus grew less well than its parent, UW-CamNS, and showed no significant difference relative to the growth of PR8(UW)/VN1194H5N1.

In addition, an Asn-to-Glu substitution at position 101 (UW-D101EUWNS1) did not yield a viral titer significantly different from that of PR8(UW)/VN1194H5N1. These results indicate that the amino acid at position 55 of NS1 affects virus growth in MDCK cells.

NS1 is known to mediate type I IFN antagonism to affect viral growth in host cells (5). We therefore analyzed the IFN antagonistic properties of each NS1 by use of an IFN bioassay to understand the molecular basis of the contribution of NS1 to the growth properties of virus in MDCK cells. In our IFN bioassay, the supernatant from MDCK cells infected with either virus possessing Glu at position 55 of NS1 (UW-K55EUWNS1 or UW-CamNS) was less able to inhibit VSV-ΔG*-GFP replication than was supernatant from cells infected with PR8(UW)/VN1194H5N1 ($P < 0.05$) (Fig. 4B). In contrast, inhibition levels were similar among viruses possessing Lys at position 55 of NS1 [PR8(UW)/VN1194H5N1, UW-E55KCamNS1, and UW-D101EUWNS1]. These results indicate that Glu at position 55 of NS1 is responsible for the enhanced type I IFN antagonistic property of PR8(Cambridge) NS1, leading to high growth in MDCK cells of viruses possessing this protein.

Alteration of the HA/NA functional balance enhances viral growth in MDCK cells. To see if we could further enhance viral growth in MDCK cells, we next determined the optimal functional balance between H5 NA and N1 NA. To this end, we produced a series of 6:2 (or 7:1) reassortants with the PR8(UW) background possessing H5 mHA derived from VN1194 or VN1203 and NAs derived from several N1 strains and compared the plaque sizes of each virus as an indicator of growth in MDCK cells (Fig. 5). The plaque size of PR8(UW)/VN1203H5N1 was 2.07 ± 0.59 mm (in diameter), which was significantly larger than that of PR8(UW)/VN1194H5N1 (1.57 ± 0.51 mm) ($P < 0.01$). We therefore used VN1203 mHA-bearing viruses for further assessments. Reassortant viruses bearing NAs from VN1203Fill or HK213 (containing a 20-amino-acid insertion in its stalk) formed significantly larger plaques (2.91 ± 0.42 or 2.83 ± 0.29 mm, respectively) than PR8(UW)/VN1203H5N1. In contrast, reassortants with NAs from the Kanagawa or PR8 strains formed smaller plaques (1.21 ± 0.31 or 0.93 ± 0.21 mm, respectively) than PR8(UW)/VN1203H5N1. Moreover, reassortants with NAs from WSN [PR8(UW)-VN1203H5/WSNN1] or NIBRG-14 formed even smaller plaques (0.53 ± 0.12 or 0.44 ± 0.09 mm, respectively). These results suggest that the HA/NA functional balance optimal for virus growth in MDCK cells is achieved by the combination of VN1203 mHA and NA with a longer stalk, such as HK213 NA or VN1203Fill NA.

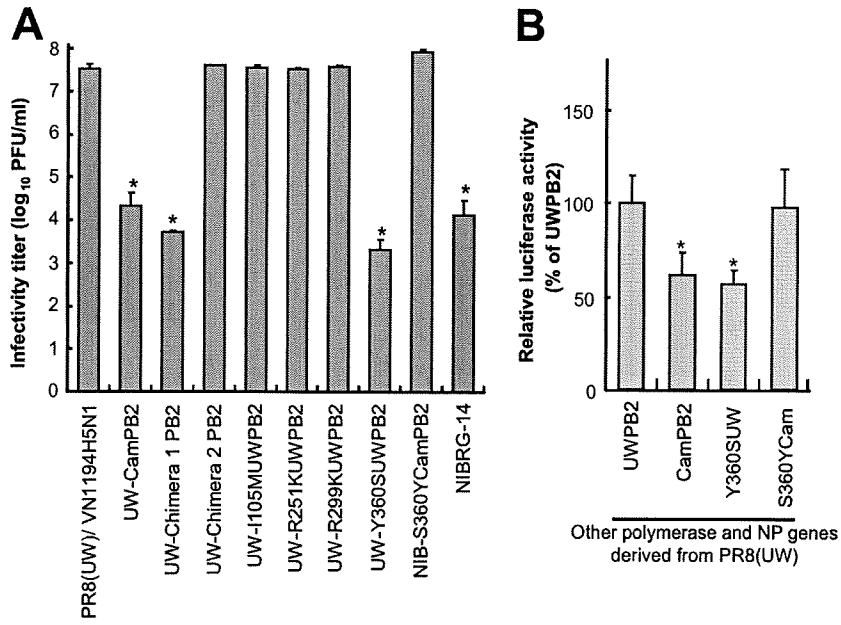

FIG. 3. Growth of PB2 mutant viruses and their polymerase activities. (A) MDCK cells were infected with PB2 mutant virus at an MOI of 0.01. UW- indicates a PR8(UW)/VN1194H5N1 background PB2 mutant, and NIB- indicates an NIBRG-14 background PB2 mutant [e.g., UW-I105MUWPB2 contains the I105M mutant of PR8(UW) PB2 in the PR8(UW)/VN1194H5N1 background]. Chimera 1 possesses the N-terminal portion of PR8(Cambridge)PB2 and the C-terminal portion of PR8(UW) PB2; chimera 2 possesses the opposite configuration. Virus titers were determined in a plaque assay with MDCK cells at 36 hpi. Titers significantly ($P < 0.05$) decreased (*) compared with that of the PR8(UW)/VN1194H5N1 virus are shown. (B) Polymerase activities with wild-type PR8(UW) PB2 and mutant PB2s were analyzed by use of a luciferase reporter assay. Wild-type or mutant PB2 was cotransfected into MDCK cells by using plasmids expressing PB1, PA, and NP of PR8(UW) plus a reporter plasmid expressing the firefly luciferase gene in the virus RNA under the control of the canine PolI promoter. At 24 h posttransfection, cells were subjected to the dual-luciferase assay. Polymerase activities, represented as ratios of firefly to *Renilla* luciferase (as an internal control) and normalized to levels for PR8(UW) PB2 transfected samples, are shown. Polymerase activities significantly ($P < 0.05$) decreased (*) compared with that of PR8(UW) PB2 are shown. The data are presented as mean values with standard deviations for three independent experiments.

Enhanced growth of the PR8/H5N1 6:2 reassortant in MDCK cells. To test if the growth-enhancing activity of NS1 and HA/NA functional balance are additive, we generated 6:2 reassortant viruses possessing heterologous NS or NA with VN1203 mHA and assessed their growth in MDCK cells (Fig. 6A). Viruses bearing the long-stalk NA, PR8(UW)/VN1203H5/VN1203FillN1 and PR8(UW)/VN1203H5/HK213N1, grew to $1.3 \times 10^8 \pm 0.5 \times 10^8$ and $1.1 \times 10^8 \pm 0.4 \times 10^8$ PFU/ml, respectively, both of which titers were significantly higher than those of viruses possessing the short-stalk NA [PR8(UW) NA or VN1203 NA]. Replacement of the NS gene of these viruses with that from PR8(Cambridge) [PR8(UW)/VN1203H5/VN1203FillN1-CamNS or PR8(UW)/VN1203H5/HK213N1-CamNS, respectively] further enhanced viral growth significantly, compared with the levels for the parental viruses ($2.33 \times 10^8 \pm 0.27 \times 10^8$ and $2.35 \times 10^8 \pm 0.21 \times 10^8$ PFU/ml, respectively).

To authenticate the enhanced viral growth in MDCK cells mediated by NS and HA/NA functional balance, we produced reassortants with other H5 mHAs derived from clade 1 (VN30259 and VN3030), clade 2.1.3 (Indo3006), and clade 2.3.4 (AH2) H5N1 viruses with similar gene constellations (Fig. 6B). Each virus showed significantly enhanced growth with the introduction of the HK213 NA gene and even greater enhancement with the introduction of the PR8(Cambridge) NS gene. These results demonstrate the universal contribution of NS1 and HA/NA functional balance to the enhanced growth of H5N1 vaccine seed viruses in MDCK cells.

DISCUSSION

In this study, we addressed the molecular determinants for growth of H5N1 vaccine seed virus in MDCK cells, which are approved for human vaccine production. Seed viruses that provide robust growth in cell culture are needed to ensure an adequate supply of H5N1 vaccine either as a supplemental to or as an alternative method for egg-based vaccine production. The H5N1 influenza vaccine seed virus that we produced and optimized for MDCK cells was a PR8/H5N1 6:2 reassortant, the internal genes of which, with the exception of the NS gene, were derived from the PR8(UW) strain. Its NS gene was derived from the PR8(Cambridge) strain and its NA gene from the HK213 strain, and its mHA gene came from a circulating H5N1 virus.

We previously reported that seed viruses with our laboratory-maintained PR8(UW) strain as the background exhibit superior growth compared to the WHO-recommended NIBRG-14 seed virus in embryonated chicken eggs (four- to sevenfold enhancement) (10). In eggs, each polymerase and NP gene of the PR8(UW) strain enhanced virus growth slightly, but when combined, all four genes contributed to the superior growth of viruses possessing the PR8(UW) genes compared to those

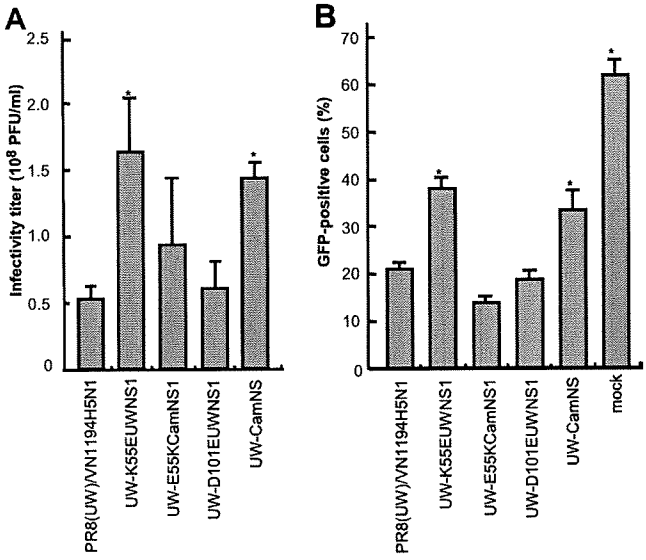

FIG. 4. Growth of NS1 mutant viruses and their IFN antagonism. (A) MDCK cells were infected with NS1 mutant viruses at an MOI of 0.01. UW- indicates a PR8(UW)/VN1194H5N1 background NS mutant [e.g., UW-E55KcamNS1 contains the E55K mutant of PR8(Cambridge)NS1 in the PR8(UW)/VN1194H5N1 background]. Virus titers were determined in a plaque assay with MDCK cells (PFU/ml) at 36 hpi. The data are shown as mean titers with standard deviations ($n \geq 3$). Titers significantly ($P < 0.05$) increased (*) compared with that of the PR8(UW)/VN1194H5N1 virus are shown. (B) A72 cells (13) were pretreated for 24 h with UV-inactivated supernatants from MDCK cells infected with the NS1 wild-type and mutant viruses. The pretreated A72 cells were then infected with VSV-ΔG*-GFP, and at 12 hpi, the number of GFP-positive cells was counted by fluorescence-activated cell sorting analysis. The data are shown as mean values with standard deviations ($n = 3$). Numbers of GFP-positive cells significantly ($P < 0.05$) increased (*) compared with that observed following treatment of the PR8(UW)/VN1194H5N1-infected cell supernatant are shown.

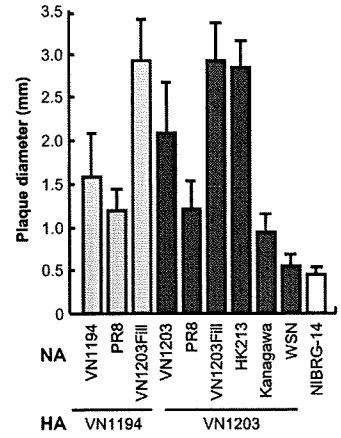

FIG. 5. Plaque sizes of PR8/H5N1 6:2 reassortant viruses. Plaque sizes of viruses containing mHA from either VN1194 or VN1203, NA from either H5N1 viruses (VN1194, VN1203, HK213, or VN1203Fill) or H1N1 viruses (PR8, Kanagawa, or WSN), and the remaining genes, which were from PR8(UW), were determined. The plaque size of NIBRG-14 is also shown. The data are reported as mean plaque diameters with standard deviations for >15 plaques with each virus.

possessing the PR8(Cambridge) genes. In MDCK cells, however, the superior viral growth (more than 1,000-fold enhancement) was essentially determined by a single-amino-acid difference at position 360 of PB2, with an additional minor contribution from NS1 (Fig. 2 and 3). Therefore, the amino acid at position 360 of PB2 is a determinant for virus growth in MDCK cells but not in eggs. It may be that this amino acid is involved in host range determinants of avian and mammalian species, which are mediated by the host factors of each animal, as previously reported for the amino acids at positions 627 and 701 of PB2 (18, 29). Theoretically, an approximately 2-fold enhancement in polymerase activity caused by the amino acid difference at position 360 of PB2 could result in a >1,000-fold increase in overall viral growth with multiple replication cycles in an exponential manner; however, additional, unknown factors may also be involved in this growth enhancement.

Here, we showed that Glu at position 55 of NS1 mediates growth enhancement of vaccine seed viruses in MDCK cells via its IFN antagonistic action (Fig. 4). In addition, we found that the growth enhancement mediated by the PR8(Cambridge) NS gene was not observed in Vero cells, which lack the type I IFN genes (3) (data not shown). There are two possible explanations for this observation; one is that the K55E substitution of NS1 may enhance the productivity of this protein in this cell line, via its increased interaction with host-cell molecules, such as chaperons, which can precisely hold and rapidly transport NS1. The other is that this substitution may increase the intrinsic IFN antagonism of NS1. The region of NS1 from position 1 to 73 is believed to be an RNA-binding site (26) that exhibits IFN antagonism by binding host mRNA and reducing the signaling for IFN gene activation at a posttranscriptional level (20, 33). Given that position 55 of NS1 lies in this RNA-binding region, NS1 that possesses E55 may have a higher affinity for host mRNAs than NS1 with K55, resulting in the enhanced inhibition of IFN gene expression that we observed in MDCK cells.

There are several PR8 strains maintained in different laboratories. The present study, together with a database search, indicated that only the PR8(Cambridge) strain possesses S360 in PB2, whereas all the others possess Y360, as does the PR8(UW) strain. On the other hand, E55 in NS1 is not limited to the PR8(Cambridge) strain. For example, the PR8(Mt. Sinai) strain possesses E55 in NS1 as well as Y360 in PB2. Thus, comparative growth evaluations and selection of a vaccine donor virus among the PR8 strains would be valuable in the future for pandemic preparedness to increase vaccine productivity.

HA/NA functional balance is another important determinant for virus growth (19, 21). The stalk length of NA correlates with its biological activity (1, 4). The NAs of HK213 and VN1203Fill bear long stalks (44 amino acids in length), which probably enhance the functionality of NA compared to NAs bearing stalk lengths of 24 amino acids, which are observed in most H5N1 viruses. Our H5N1 seed viruses with long-stalk NAs grew better than those bearing homologous N1 NAs in MDCK cells, suggesting that the HA/NA functional balance of viruses with long-stalk NAs is superior to that of those viruses with short-stalk NAs for growth in this cell line. Recently, we reported that disrupting HA/NA functional balance by replacing the NA gene with PR8 NA enhances the growth of H5N1

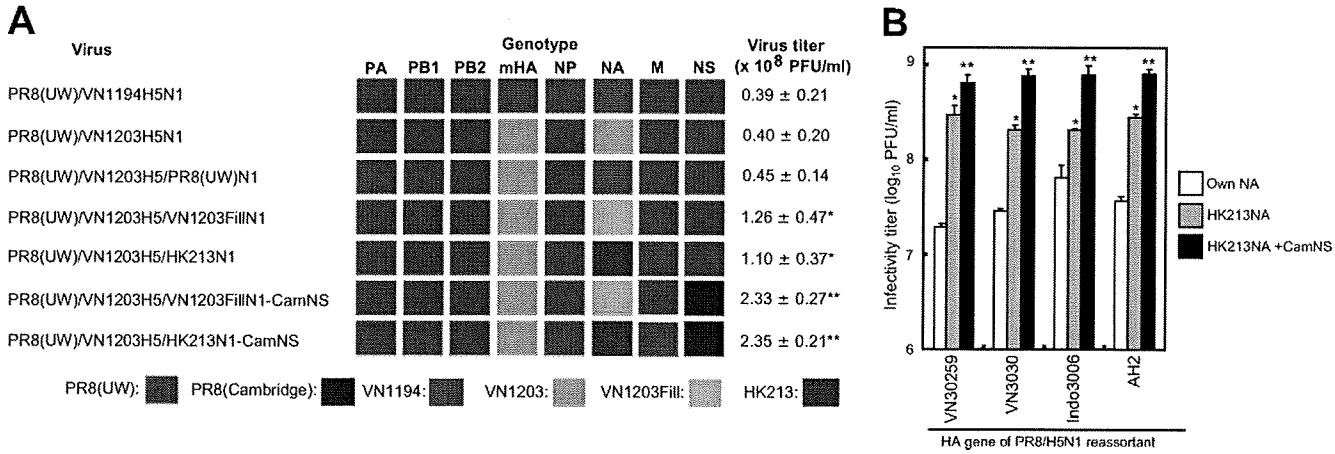

FIG. 6. Growth enhancement of a PR8/H5N1 reassortant mediated by NA and NS genes. (A) MDCK cells were infected with reassortant viruses containing mHA from either VN1194 or VN1203 and NA from a different N1 virus or NS from PR8(Cambridge) at an MOI of 0.01. Virus titers were determined in a plaque assay with MDCK cells at 36 hpi. The data are reported as mean titers with standard deviations for three independent experiments. Titers significantly ($P < 0.05$) increased (*) compared with that of the PR8(UW)/VN1194H5N1 virus are shown and compared with those of PR8(UW)/VN1203H5/VN1203FillN1 and PR8(UW)/VN1203H5/HK213N1 (**). (B) MDCK cells were infected with reassortant viruses containing H5 mHA from clade 1 and clade 2 strains with homologous NA or HK213 NA or PR8(Cambridge) NS instead of PR8(UW) NS at an MOI of 0.01. Virus titers were determined in a plaque assay with MDCK cells at 36 hpi. The data are reported as mean titers with standard deviations for three independent experiments. Titers significantly ($P < 0.05$) increased compared with those of the viruses possessing homologous NA (*) or compared with those of viruses possessing HK213 NA (**) are shown.

vaccine seed viruses in eggs (10). In this study, optimized HA/NA functional balance in MDCK cells differed from that in eggs, possibly due to a difference in cell receptors between these two substrates.

In our previous report, we discussed, albeit to a limited extent, the possibility of a reduction in the protective immunity of the vaccine seeds due to the inclusion of heterologous N1 NAs (10). In this context, the seed virus with artificial VN1203Fill NA would fare better than that with HK213 NA. However, a recent report showed considerable cross-protective immunogenicity between N1s from human H1N1 and H5N1 viruses in a mouse model (28). Therefore, we believe that inclusion of heterologous N1 NAs in the seed viruses would provide an advantage for vaccine supply, which would likely offset the limited antigenic mismatch in this minor antigen.

It is well known that the HA antigenicities of human H3N2 and H1N1 influenza viruses readily change following propagation in eggs (15, 27). This occurs because of differences in the cell receptors expressed in eggs (12). However, MDCK cells contain both avian- and human-type receptors (12), which circumvents any HA antigenic changes in the H5N1 vaccine seed viruses.

In conclusion, we propose a seed virus for MDCK cell-based H5N1 vaccine production in the form of a 6:2 reassortant that possesses mHA from a circulating H5N1 virus, NA from HK213, and its remaining genes from the PR8(UW) strain, except for the NS gene, which comes from the PR8(Cambridge) strain. A cell culture-based strategy with this seed virus would allow increased production of prepandemic or pandemic inactivated H5N1 vaccines in a timely, cost-efficient manner as a supplement or an alternative to egg-based vaccine production.

ACKNOWLEDGMENTS

We thank J. M. Wood and J. S. Robertson (National Institute for Biological Standards and Control, United Kingdom) for providing NIBRG-14 virus, Michael Whitt for providing VSV-ΔG*-GFP virus, and S. Watson for editing the manuscript.

This work was supported in part by grants-in-aid for Specially Promoted Research and for Scientific Research (B) from the Ministry of Education, Culture, Sports, Science, and Technology, Japan; by a grant for Scientific Research from the Ministry of Health, Labor, and Welfare, Japan; by CREST (Core Research for Evolutional Science and Technology), Japan; by a contract research fund for the Program of Founding Research Centers for Emerging and Reemerging Infectious Diseases from the Ministry of Education, Culture, Sports, Science and Technology, Japan; and by research grants from the U.S. Public Health Service, National Institute of Allergy and Infectious Diseases.

REFERENCES

1. **Castrucci, M., and Y. Kawaoka.** 1993. Biologic importance of neuraminidase stalk length in influenza A virus. J. Virol. **67**:759–764.
2. **Dennis, C.** 2006. Flu-vaccine makers toil to boost supply. Nature **440**:1099.
3. **Diaz, M., S. Ziemin, M. Le Beau, P. Pitha, S. Smith, R. Chilcote, and J. Rowley.** 1988. Homozygous deletion of the alpha- and beta 1-interferon genes in human leukemia and derived cell lines. Proc. Natl. Acad. Sci. USA **85**:5259–5263.
4. **Els, M. C., G. M. Air, K. G. Murti, R. G. Webster, and W. G. Laver.** 1985. An 18-amino acid deletion in an influenza neuraminidase. Virology **142**:241–247.
5. **García-Sastre, A., and C. Biron.** 2006. Type 1 interferons and the virus-host relationship: a lesson in détente. Science **312**:879–882.
6. **Genzel, Y., M. Fischer, and U. Reichl.** 2006. Serum-free influenza virus production avoiding washing steps and medium exchange in large-scale microcarrier culture. Vaccine **24**:3261–3272.
7. **Govorkova, E., S. Kodihalli, I. Alymova, B. Fanget, and R. Webster.** 1999. Growth and immunogenicity of influenza viruses cultivated in Vero or MDCK cells and in embryonated chicken eggs. Dev. Biol. Stand. **98**:39–51, 73–74.
8. **Halperin, S., B. Smith, T. Mabrouk, M. Germain, P. Trépanier, T. Hassell, J. Treanor, R. Gauthier, and E. Mills.** 2002. Safety and immunogenicity of a trivalent, inactivated, mammalian cell culture-derived influenza vaccine in healthy adults, seniors, and children. Vaccine **20**:1240–1247.
9. **Horimoto, T., and Y. Kawaoka.** 2005. Influenza: lessons from past pandemics, warnings from current incidents. Nat. Rev. Microbiol. **3**:591–600.
10. **Horimoto, T., S. Murakami, Y. Muramoto, S. Yamada, K. Fujii, M. Kiso, K. Iwatsuki-Horimoto, Y. Kino, and Y. Kawaoka.** 2007. Enhanced growth of seed viruses for H5N1 influenza vaccines. Virology **366**:23–27.
11. **Horimoto, T., A. Takada, K. Fujii, H. Goto, M. Hatta, S. Watanabe, K. Iwatsuki-Horimoto, M. Ito, Y. Tagawa-Sakai, S. Yamada, H. Ito, T. Ito, M. Imai, S. Itamura, T. Odagiri, M. Tashiro, W. Lim, Y. Guan, M. Peiris, and**

Y. Kawaoka. 2006. The development and characterization of H5 influenza virus vaccines derived from a 2003 human isolate. Vaccine 24:3669–3676.
12. Ito, T., Y. Suzuki, A. Takada, A. Kawamoto, K. Otsuki, H. Masuda, M. Yamada, T. Suzuki, H. Kida, and Y. Kawaoka. 1997. Differences in sialic acid-galactose linkages in the chicken egg amnion and allantois influence human influenza virus receptor specificity and variant selection. J. Virol. 71:3357–3362.
13. Iwata, A., N. M. Iwata, T. Saito, K. Hamada, Y. Sokawa, and S. Ueda. 1996. Cytopathic effect inhibition assay for canine interferon activity. J. Vet. Med. Sci. 58:23–27.
14. James, J., R. Zeiger, M. Lester, M. Fasano, J. Gern, L. Mansfield, H. Schwartz, H. Sampson, H. Windom, S. Machtinger, and S. Lensing. 1998. Safe administration of influenza vaccine to patients with egg allergy. J. Pediatr. 133:624–628.
15. Katz, J., C. Naeve, and R. Webster. 1987. Host cell-mediated variation in H3N2 influenza viruses. Virology 156:386–395.
16. Katz, J., and R. Webster. 1992. Amino acid sequence identity between the HA1 of influenza A (H3N2) viruses grown in mammalian and primary chick kidney cells. J. Gen. Virol. 73:1159–1165.
17. Kobasa, D., A. Takada, K. Shinya, M. Hatta, P. Halfmann, S. Theriault, H. Suzuki, H. Nishimura, K. Mitamura, N. Sugaya, T. Usui, T. Murata, Y. Maeda, S. Watanabe, M. Suresh, T. Suzuki, Y. Suzuki, H. Feldmann, and Y. Kawaoka. 2004. Enhanced virulence of influenza A viruses with the haemagglutinin of the 1918 pandemic virus. Nature 431:703–707.
18. Li, Z., H. Chen, P. Jiao, G. Deng, G. Tian, Y. Li, E. Hoffmann, R. Webster, Y. Matsuoka, and K. Yu. 2005. Molecular basis of replication of duck H5N1 influenza viruses in a mammalian mouse model. J. Virol. 79:12058–12064.
19. Lu, B., H. Zhou, D. Ye, G. Kemble, and H. Jin. 2005. Improvement of influenza A/Fujian/411/02 (H3N2) virus growth in embryonated chicken eggs by balancing the hemagglutinin and neuraminidase activities, using reverse genetics. J. Virol. 79:6763–6771.
20. Ludwig, S., X. Wang, C. Ehrhardt, H. Zheng, N. Donelan, O. Planz, S. Pleschka, A. García-Sastre, G. Heins, and T. Wolff. 2002. The influenza A virus NS1 protein inhibits activation of Jun N-terminal kinase and AP-1 transcription factors. J. Virol. 76:11166–11171.
21. Mitnaul, L., M. Matrosovich, M. Castrucci, A. Tuzikov, N. Bovin, D. Kobasa, and Y. Kawaoka. 2000. Balanced hemagglutinin and neuraminidase activities are critical for efficient replication of influenza A virus. J. Virol. 74:6015–6020.
22. Murakami, S., T. Horimoto, S. Yamada, S. Kakugawa, H. Goto, and Y. Kawaoka. 2008. Establishment of canine RNA polymerase I-driven reverse genetics for influenza A virus: its application for H5N1 vaccine production. J. Virol. 82:1605–1609.
23. Neumann, G., T. Watanabe, H. Ito, S. Watanabe, H. Goto, P. Gao, M. Hughes, D. Perez, R. Donis, E. Hoffmann, G. Hobom, and Y. Kawaoka. 1999. Generation of influenza A viruses entirely from cloned cDNAs. Proc. Natl. Acad. Sci. USA 96:9345–9350.
24. Ozawa, M., K. Fujii, Y. Muramoto, S. Yamada, S. Yamayoshi, A. Takada, H. Goto, T. Horimoto, and Y. Kawaoka. 2007. Contributions of two nuclear localization signals of influenza A virus nucleoprotein to viral replication. J. Virol. 81:30–41.
25. Park, M. S., M. L. Shaw, J. Muñoz-Jordan, J. F. Cros, T. Nakaya, N. Bouvier, P. Palese, A. García-Sastre, and C. F. Basler. 2003. Newcastle disease virus (NDV)-based assay demonstrates interferon-antagonist activity for the NDV V protein and the Nipah virus V, W, and C proteins. J. Virol. 77:1501–1511.
26. Qian, X., C. Chien, Y. Lu, G. Montelione, and R. Krug. 1995. An amino-terminal polypeptide fragment of the influenza virus NS1 protein possesses specific RNA-binding activity and largely helical backbone structure. RNA 1:948–956.
27. Robertson, J., J. Bootman, R. Newman, J. Oxford, R. Daniels, R. Webster, and G. Schild. 1987. Structural changes in the haemagglutinin which accompany egg adaptation of an influenza A(H1N1) virus. Virology 160:31–37.
28. Sandbulte, M., G. Jimenez, A. Boon, L. Smith, J. Treanor, and R. Webby. 2007. Cross-reactive neuraminidase antibodies afford partial protection against H5N1 in mice and are present in unexposed humans. PLoS Med. 4:e59.
29. Subbarao, E., W. London, and B. Murphy. 1993. A single amino acid in the PB2 gene of influenza A virus is a determinant of host range. J. Virol. 67:1761–1764.
30. Takada, A., C. Robison, H. Goto, A. Sanchez, K. Murti, M. Whitt, and Y. Kawaoka. 1997. A system for functional analysis of Ebola virus glycoprotein. Proc. Natl. Acad. Sci. USA 94:14764–14769.
31. Treanor, J., J. Campbell, K. Zangwill, T. Rowe, and M. Wolff. 2006. Safety and immunogenicity of an inactivated subvirion influenza A (H5N1) vaccine. N. Engl. J. Med. 354:1343–1351.
32. Ulmer, J., U. Valley, and R. Rappuoli. 2006. Vaccine manufacturing: challenges and solutions. Nat. Biotechnol. 24:1377–1383.
33. Wang, X., M. Li, H. Zheng, T. Muster, P. Palese, A. Beg, and A. García-Sastre. 2000. Influenza A virus NS1 protein prevents activation of NF-κB and induction of alpha/beta interferon. J. Virol. 74:11566–11573.
34. Wood, J., and J. Robertson. 2004. From lethal virus to life-saving vaccine: developing inactivated vaccines for pandemic influenza. Nat. Rev. Microbiol. 2:842–847.

blood

2009 113: 1071-1074
Prepublished online Oct 27, 2008;
doi:10.1182/blood-2008-07-166363

Gene expression profiling of peripheral T-cell lymphoma including {gamma}{delta} T-cell lymphoma

Kana Miyazaki, Motoko Yamaguchi, Hiroshi Imai, Tohru Kobayashi, Satoshi Tamaru, Kazuhiro Nishii, Masao Yuda, Hiroshi Shiku and Naoyuki Katayama

Blood (print ISSN 0006-4971, online ISSN 1528-0020), is published semimonthly by the American Society of Hematology, 1900 M St, NW, Suite 200, Washington DC 20036.

Brief report

Gene expression profiling of peripheral T-cell lymphoma including γδ T-cell lymphoma

Kana Miyazaki,[1] Motoko Yamaguchi,[1] Hiroshi Imai,[2] Tohru Kobayashi,[1] Satoshi Tamaru,[1] Kazuhiro Nishii,[1] Masao Yuda,[3] Hiroshi Shiku,[4] and Naoyuki Katayama[1]

Departments of [1]Hematology and Oncology, [2]Pathologic Oncology, [3]Medical Zoology, and [4]Cancer Vaccine and Immuno-Gene Therapy, Mie University Graduate School of Medicine, Tsu, Japan

The gene expression profile of peripheral γδ T-cell lymphoma (γδTCL) has not been investigated. Using oligonucleotide microarrays, we analyzed total RNA from 7 patients with γδTCL (4 hepatosplenic, 1 cutaneous, 1 intestinal, and 1 thyroidal) and 27 patients with αβTCL (11 peripheral TCL-unspecified, 15 angioimmunoblastic TCL, and 1 hepatosplenic). Unsupervised microarray analyses classified all hepatosplenic γδTCLs into a single cluster, whereas other γδTCLs were scattered within the αβTCL distribution. We identified a T-cell receptor signature gene set, which accurately classified γδTCL and αβTCL. A classifier based on gene expression under supervised analysis correctly identified γδTCL. One case of hepatosplenic αβTCL was placed in the γδTCL grouping. γδTCL signature genes included genes encoding killer cell immunoglobulin-like receptors and killer cell lectin-like receptors. Our results indicate that hepatosplenic γδTCL is a distinct form of peripheral TCL and suggest that nonhepatosplenic γδTCLs are heterogeneous in gene expression. (Blood. 2009;113:1071-1074)

Introduction

T cells expressing the γδ T-cell receptor (TCR) heterodimer comprise only a small fraction of the peripheral blood T-cell population and differ from those expressing the αβ TCR in terms of development, tissue distribution, and function.[1,2] Mature T-cell lymphomas (TCLs) with the γδ T-cell immunophenotype can be divided into hepatosplenic γδTCL[3] and nonhepatosplenic γδTCL.[4] The third World Health Organization (WHO) classification system describes hepatosplenic γδTCLs and hepatosplenic αβTCLs as a single disease entity (hepatosplenic TCL) as they exhibit nearly identical clinicopathologic and cytogenetic features.[4-6]

In contrast, nonhepatosplenic γδTCL occurs in only a limited number of anatomic sites, including cutaneous, nasopharyngeal, gastrointestinal, pulmonary, and thyroidal regions.[7-10] This disease has also been called mucocutaneous γδTCL because the majority of patients show some involvement of mucocutaneous sites. Among nonhepatosplenic γδTCLs, the cutaneous form is most common and overlaps with subcutaneous panniculitis-like TCL.[11,12] Whereas primary cutaneous γδTCL is categorized as a single disease entity in the new WHO scheme,[13] other nonhepatosplenic γδTCLs remains an enigma.

γδTCLs are rare lymphoid malignancies and are difficult to diagnose, resulting from the lack of available monoclonal antibodies against γδTCR for use with paraffin-embedded tissue. Several studies have elucidated the gene expression profile of peripheral TCLs (PTCLs)[14-17] but did not evaluate γδTCL. In our current study, we performed gene expression profiling in 34 PTCLs, including 7 cases of γδTCL.

Methods

Patients/samples

Our present study assessed 34 cases of PTCL, including 11 PTCL-unspecified with αβ T-cell immunophenotype, 15 angioimmunoblastic TCLs, 1 hepatosplenic αβTCL, 4 hepatosplenic γδTCLs, 1 cutaneous γδTCL, 1 intestinal γδTCL, and 1 thyroidal γδTCL. All specimens were collected between 1987 and 2002 at Mie University Hospital and diagnosed according to the third WHO classification.[6] Tumor cell expression of cell-surface antigens and TCR heterodimer (αβ or γδ) was confirmed by immunohistochemistry using frozen sections as described previously.[9] DNA microarray studies using specimens from patients with hematopoietic malignancies were approved by the Institutional Review Committee of Mie University Graduate School of Medicine. Informed consent was obtained from these patients in accordance with the Declaration of Helsinki. The clinicopathologic features of 6 of 7 cases of γδTCL have been reported previously.[8,9] The single patient we examined with thyroidal γδTCL remains alive with no evidence of disease 13 years after diagnosis. Clinical data for all cases examined are presented in Table S1 (available on the *Blood* website; see the Supplemental Materials link at the top of the online article).

Gene expression profiling and analysis

Gene expression profiles were generated and analyzed as previously reported.[18] We used the Agilent 44K human oligonucleotide microarray (Agilent 4112F; Agilent Technologies, Palo Alto, CA), and raw gene expression data are available at the Gene Expression Omnibus (accession number GSE11946).[19] For gene expression profiling supervised by TCR heterodimer phenotype, we selected genes with an average differential expression level of more than 3.0-fold and used a one-sample *t* test with a

Submitted July 10, 2008; accepted October 11, 2008. Prepublished online as *Blood* First Edition paper, October 27, 2008; DOI 10.1182/blood-2008-07-166363.

The online version of this article contains a data supplement.

Presented in part at the Tenth International Conference on Malignant Lymphoma, Lugano, Switzerland, June 4, 2008.

The publication costs of this article were defrayed in part by page charge payment. Therefore, and solely to indicate this fact, this article is hereby marked "advertisement" in accordance with 18 USC section 1734.

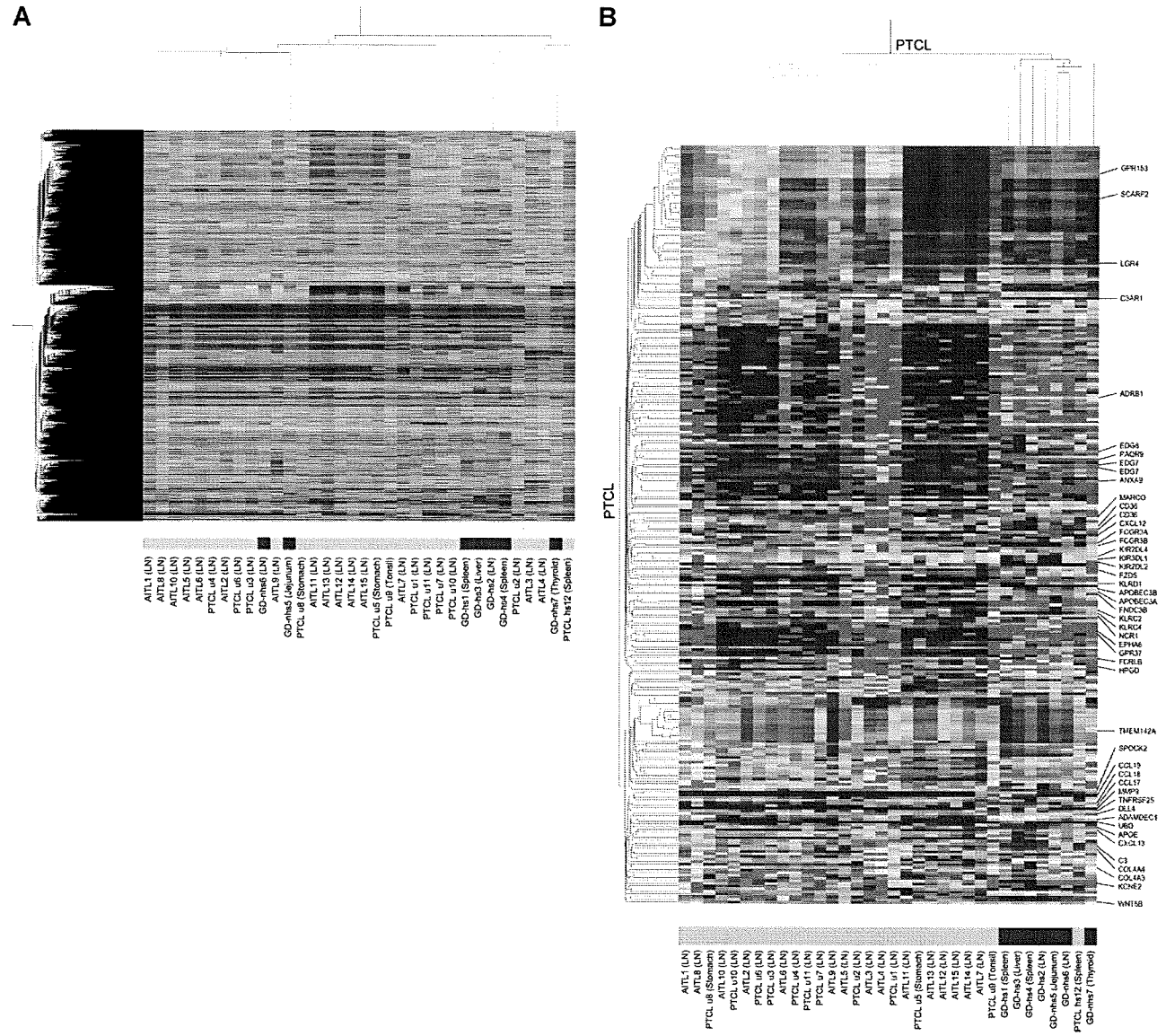

Figure 1. Hierarchical clustering of gene expression data. (A) Hierarchical clustering of 34 cases of PTCL using unsupervised analysis. Color blocks indicate the characteristics of the PTCLs; red blocks, γδTCL cases; amber blocks, αβTCL cases. The anatomic site of each specimen is shown in parentheses. AITL indicates angioimmunoblastic TCL; GD-hs, hepatosplenic γδTCL; GD-nhs, nonhepatosplenic γδTCL; LN, lymph node; PTCL hs, hepatosplenic αβTCL; PTCL u, PTCL-unspecified. Four cases of hepatosplenic γδTCL (GD-hs1-4) were classified into a single cluster. Nonhepatosplenic γδTCLs (GD-nhs5, intestinal; GD-nhs6, cutaneous; GD-nhs7, thyroidal) were scattered within the αβTCL distribution. (B) Hierarchical clustering of 34 cases of PTCL-based TCR signature gene expression. Genes also listed in Table 1 are shown on the right. γδTCL cases were correctly identified by the gene set, although one case of hepatosplenic αβTCL (PTCL hs12) was grouped with the γδTCLs.

P value cutoff of .005. Hierarchical clustering of genes was performed using the Pearson correlation, and hierarchical clustering of cases was obtained using an average linkage algorithm.

We chose WebGestalt using Gene Ontology (GO) hierarchies[20,21] for categorization of functional gene groups and the Kyoto Encyclopedia of Genes and Genomes (KEGG)[22,23] pathway for identification of signaling pathways. In both analyses, we performed a separate hypergeometric test with a *P* value cutoff of .001.

Results and discussion

Gene expression profiling is a powerful tool for establishing a molecular basis for lymphoma subtypes.[24] Unsupervised analysis of our PTCL cases classified hepatosplenic γδTCL as a single cluster, whereas other γδTCLs were scattered within the αβTCL distribution (Figure 1A). Since the 1980s, cumulative clinicopathologic evidence has demonstrated that hepatosplenic γδTCL is a distinct clinicopathologic disease entity. Our gene expression results also confirm that hepatosplenic γδTCL is distinct from other PTCLs. Conversely, nonhepatosplenic γδTCLs appeared to be more heterogeneous. The possibility that tissue differences were responsible for these data was excluded by our observation that hepatosplenic γδTCL was classified as a single cluster, irrespective of the specimen examined (Figure 1). Angioimmunoblastic TCL cases were not classified as a single cluster, consistent with prior gene expression studies.[14-17]

We next compared the gene expression profiles of γδTCL and αβTCL using 291 genes showing a greater than 3.0-fold average expression difference, which we designated the TCR signature gene set (Table S2). Of note, a classifier from supervised analysis based on gene expression identified γδTCL and hepatosplenic αβTCL (Figure 1B). This finding is supported by the notion that γδ

Table 1. GO category analysis and KEGG pathway analysis in the TCR signature gene set

Analytical tool	Gene no.	Gene	P
GO category			
γδTCL			
Cellular defense response	5	*KIR2DL4, NCR1, C3AR1, KLRC2, KLRC4*	1.17×10^{-4}
Signal transduction activity	29	*KLRD1, ANXA9, FNDC3B, GPR37, KIR2DL4, MARCO, EDG7, NCR1, MS4A5, HPGD, FCGR3A, LGR4, FCRLB, C3AR1, CXCL12, RTN4R, PAQR9, KLRC2, GPR153, FCGR3B, KIR2DL2, EDG8, ADRB1, CD36, FZD5, SCARF2, KIR3DL1, EPHA6, KLRC4*	5.09×10^{-6}
Receptor activity	28	*GPR37, KIR2DL4, ANXA9, KLRD1, FNDC3B, EDG7, HPGD, MARCO, LGR4, MS4A5, FCGR3A, NCR1, C3AR1, FCRLB, KLRC2, PAQR9, RTN4R, GPR153, EDG8, FCGR3B, KIR2DL2, ADRB1, FZD5, CD36, SCARF2, KIR3DL1, EPHA6, KLRC4*	7.10×10^{-8}
Transmembrane receptor activity	16	*ANXA9, GPR37, KIR2DL4, KLRD1, LGR4, HPGD, MARCO, EDG7, C3AR1, KLRC2, EDG8, GPR153, ADRB1, FZD5, EPHA6, KIR3DL1*	4.46×10^{-4}
IgG binding	2	*FCGR3A, FCGR3B*	3.07×10^{-4}
αβTCL			
Organismal physiologic process	14	*UBD, CXCL13, COL4A4, CCL18, KCNE2, CCL17, C3, TMEM142A, DLL4, APOE, COL4A3, TNFRSF25, MMP9, CCL19*	3.24×10^{-4}
Regulation of organismal physiologic process	4	*COL4A4, KCNE2, C3, APOE*	5.87×10^{-4}
Circulation	4	*KCNE2, DLL4, COL4A3, APOE*	3.14×10^{-4}
Regulation of neurophysiologic process	2	*COL4A4, APOE*	7.55×10^{-4}
Regulation of transmission of nerve impulse	2	*COL4A4, APOE*	7.55×10^{-4}
Regulation of synapse structure and function	2	*COL4A4, APOE*	8.69×10^{-4}
Regulation of synaptic transmission	2	*COL4A4, APOE*	7.55×10^{-4}
Inflammatory response	5	*CXCL13, CCL18, CCL17, C3, CCL19*	6.05×10^{-4}
Behavior	5	*CCL18, CXCL13, CCL17, APOE, CCL19*	2.47×10^{-4}
Locomotory behavior	4	*CXCL13, CCL18, CCL17, CCL19*	4.92×10^{-4}
Taxis	4	*CXCL13, CCL18, CCL17, CCL19*	4.22×10^{-4}
Chemotaxis	4	*CXCL13, CCL18, CCL17, CCL19*	4.22×10^{-4}
Receptor binding	9	*ADAMDEC1, CCL18, CXCL13, CCL17, C3, DLL4, APOE, COL4A3, CCL19*	2.76×10^{-5}
G-protein–coupled receptor binding	4	*CCL18, CXCL13, CCL17, CCL19*	1.57×10^{-5}
Chemokine receptor binding	4	*CCL18, CXCL13, CCL17, CCL19*	6.97×10^{-6}
Chemokine activity	4	*CCL18, CXCL13, CCL17, CCL19*	6.37×10^{-6}
Extracellular region	11	*CCL18, COL4A4, CXCL13, CCL17, C3, WNT5B, MMP9, COL4A3, APOE, SPOCK2, CCL19*	7.97×10^{-5}
Extracellular region part	9	*CCL18, COL4A4, CXCL13, CCL17, SPOCK2, APOE, COL4A3, MMP9, CCL19*	7.33×10^{-5}
Sheet-forming collagen	2	*COL4A4, COL4A3*	1.70×10^{-4}
Collagen type IV	2	*COL4A4, COL4A3*	1.21×10^{-4}
KEGG pathway			
γδTCL			
Natural killer cell–mediated cytotoxicity	5	*FCGR3A, KIR3DL1, KLRC2, KLRD1, NCR1*	8.10×10^{-4}
Antigen processing and presentation	4	*KIR3DL1, KLRC2, KLRD1, KLRC4*	7.53×10^{-4}
Atrazine degradation	2	*APOBEC3A, APOBEC3B*	4.42×10^{-4}
αβTCL			
Cytokine–cytokine receptor interaction	5	*CXCL13, CCL17, CCL18, CCL19, TNFRSF25*	2.65×10^{-4}

T cells partially share a cytotoxic immunophenotype with cytotoxic αβ T cells.[1,2] Among 30 patients for whom survival data were available, the prognosis for 8 cases with a γδTCL gene profile (7 γδTCLs and 1 hepatosplenic αβTCL) was not significantly poorer than that of 22 patients with an αβTCL gene profile ($P = .152$; Figure S1). The unusual case of thyroidal γδTCL in the γδTCL gene profile group may affect the result because the P value was .009 when we excluded this patient from the survival analysis (data not shown). Future analyses will probably reveal the relationship between our TCR signature gene set and prognostic indicators.

In γδTCL, genes of natural killer (NK) cell–associated molecules, such as killer cell immunoglobulin (Ig)–like receptor (KIR) genes (*KIR3DL1*, *KIR2DL4*, and *KIR2DL2*), and killer cell lectin-like receptors (*KLRC4*, *KLRD1*, and *KLRC2*) were found to be overexpressed (Figure 1; Table S2). These NK receptors are expressed by a subset of NK cells, γδ T cells, and $CD8^+$ αβ T cells.[25] KIR3DL1 and KIR2DL2 exhibit inhibitory functions, and KIR2DL4 has potentially both inhibitory and activating roles.[25] KIR3DL1, KIR2DL2, and KLRD1 are reported to be expressed in some cases of hepatosplenic γδTCL.[26,27] Although *KLRC4*, a top 10 feature gene that characterizes γδTCL and its protein, NKG2F, is expressed in human NK cells,[28] its expression in normal γδ T cells has not been determined. CD16 is also frequently expressed in cases of hepatosplenic γδTCL,[4,27] and its genes (*FCGR3B* and *FCGR3A*) were among the γδTCL signature genes identified in this study.

To search for functionally important genes overexpressed in γδTCL, we performed GO and pathway analysis using 139 of 204 and 53 of 87 known genes in the γδTCL and αβTCL groups, respectively. By WebGestalt, 5 and 20 GO categories were enriched in γδTCL and αβTCL, respectively (Table 1). The enriched GO categories in γδTCL were cellular defense response, signal transduction activity, receptor activity, transmembrane receptor activity, and IgG binding. Three γδTCL pathways and 1 αβTCL pathway were found to be altered in KEGG-signaling analyses (Table 1). No γδTCL and αβTCL signature genes were

shared in a GO category or KEGG pathway, indicating different functional profiles between γδTCL and αβTCL. Four of the 5 γδTCL-enriched GO categories and 2 of the 3 KEGG-signaling pathways altered in γδTCL contained genes encoding KIRs and killer cell lectin-like receptors, a finding that suggests that the expression of these genes may be important for the differential diagnosis of γδTCL and αβTCL.

In conclusion, our current gene expression data confirm that hepatosplenic γδTCL is a distinct lymphoma entity in PTCLs and reveal differences in the gene expression profiles of αβTCL and γδTCL. Further investigations of our newly identified TCR signature genes are warranted to identify novel therapeutic targets and facilitate the diagnosis of γδTCL.

Acknowledgments

We thank the following institutions for providing patient data: Suzuka Chuo General Hospital, Suzuka Kaisei Hospital, Mie University Hospital, Takeuchi Hospital, Tohyama Hospital, Nagai Hospital, Matsusaka Municipal Hospital, Matsusaka Chuo General Hospital, Matsusaka Saiseikai General Hospital, Yamada Red Cross Hospital, and Ise City General Hospital.

This work was supported in part by the Grants-in-Aid for Cancer Research (19-8, 17S-1, 20S-1) from the Ministry of Health, Labor and Welfare, Japan.

Authorship

Contribution: K.M. and M. Yamaguchi designed and performed the study, collected data and samples, interpreted data, and wrote the paper; H.I. and S.T. performed the study and collected samples; M. Yuda and H.S. contributed analytical tools and supervised the research; K.N. collected samples and wrote the paper; and T.K. and N.K. supervised the research and wrote the paper.

Conflict-of-interest disclosure: The authors declare no competing financial interests.

Correspondence: Motoko Yamaguchi, Department of Hematology and Oncology, Mie University Graduate School of Medicine, 2-174 Edobashi, Tsu, Mie 514-8507, Japan; e-mail: waniwani@clin.medic.mie-u.ac.jp.

References

1. Hayday AC. γδ cells: a right time and a right place for a conserved third way of protection. Annu Rev Immunol. 2000;18:975-1026.
2. Carding SR, Egan PJ. γδ T cells: functional plasticity and heterogeneity. Nat Rev Immunol. 2002; 2:336-345.
3. Farcet JP, Gaulard P, Marolleau JP, et al. Hepatosplenic T-cell lymphoma: sinusal/sinusoidal localization of malignant cells expressing the T-cell receptor γδ. Blood. 1990;75:2213-2219.
4. Vega F, Medeiros LJ, Gaulard P. Hepatosplenic and other γδ T-cell lymphomas. Am J Clin Pathol. 2007;127:869-880.
5. Macon WR, Levy NB, Kurtin PJ, et al. Hepatosplenic αβ T-cell lymphomas: a report of 14 cases and comparison with hepatosplenic γδ T-cell lymphomas. Am J Surg Pathol. 2001;25:285-296.
6. Jaffe ES, Harris NL, Stein H, Vardiman JW. World Health Organization Classification of Tumours: Pathology and Genetics of Tumours of Haematopoietic and Lymphoid Tissues. Lyon, France: International Agency for Research on Cancer; 2001.
7. Arnulf B, Copie-Bergman C, Delfau-Larue MH, et al. Nonhepatosplenic γδ T-cell lymphoma: a subset of cytotoxic lymphomas with mucosal or skin localization. Blood. 1998;91:1723-1731.
8. Yamaguchi M, Ohno T, Kita K. γ/δ T-cell lymphoma of the thyroid gland. N Engl J Med. 1997; 336:1391-1392.
9. Yamaguchi M, Ohno T, Nakamine H, et al. γδ T-cell lymphoma: a clinicopathologic study of 6 cases including extrahepatosplenic type. Int J Hematol. 1999;69:186-195.
10. Jaffe ES. Pathobiology of peripheral T-cell lymphomas. Hematology. 2006:317-322.
11. Toro JR, Liewehr DJ, Pabby N, et al. Gamma-delta T-cell phenotype is associated with significantly decreased survival in cutaneous T-cell lymphoma. Blood. 2003;101:3407-3412.
12. Willemze R, Jansen PM, Cerroni L, et al. Subcutaneous panniculitis-like T-cell lymphoma: definition, classification, and prognostic factors: an EORTC Cutaneous Lymphoma Group Study of 83 cases. Blood. 2008;111:838-845.
13. Swerdlow SH, Campo E, Harris NL, et al. WHO Classification of Tumours of Haematopoietic and Lymphoid Tissues. Lyon, France: International Agency for Research on Cancer; 2008.
14. Ballester B, Ramuz O, Gisselbrecht C, et al. Gene expression profiling identifies molecular subgroups among nodal peripheral T-cell lymphomas. Oncogene. 2006;25:1560-1570.
15. Cuadros M, Dave SS, Jaffe ES, et al. Identification of a proliferation signature related to survival in nodal peripheral T-cell lymphomas. J Clin Oncol. 2007;25:3321-3329.
16. de Leval L, Rickman DS, Thielen C, et al. The gene expression profile of nodal peripheral T-cell lymphoma demonstrates a molecular link between angioimmunoblastic T-cell lymphoma (AITL) and follicular helper T (T_{FH}) cells. Blood. 2007;109:4952-4963.
17. Piccaluga PP, Agostinelli C, Califano A, et al. Gene expression analysis of peripheral T cell lymphoma, unspecified, reveals distinct profiles and new potential therapeutic targets. J Clin Invest. 2007;117:823-834.
18. Miyazaki K, Yamaguchi M, Suguro M, et al. Gene expression profiling of diffuse large B-cell lymphoma supervised by CD21 expression. Br J Haematol. 2008;142:562-570.
19. National Center for Biotechnology Information. GEO: Gene Expression Omnibus. http://www.ncbi.nlm.nih.gov/geo/. Accessed July 1, 2008.
20. Zhang B, Kirov S, Snoddy J. WebGestalt: an integrated system for exploring gene sets in various biological contexts. Nucleic Acids Res. 2005;33: W741-W748.
21. Vanderbilt University. WebGestalt. http://bioinfo.vanderbilt.edu/webgestalt/. Accessed May 2, 2008.
22. Kanehisa M, Goto S. KEGG: Kyoto encyclopedia of genes and genomes. Nucleic Acids Res. 2000; 28:27-30.
23. Kanehisa Laboratories. KEGG: Kyoto Encyclopedia of Genes and Genomes. http://www.genome.ad.jp/kegg/. Accessed May 2, 2008.
24. Staudt LM, Dave S. The biology of human lymphoid malignancies revealed by gene expression profiling. Adv Immunol. 2005;87:163-208.
25. Lanier LL. NK cell recognition. Annu Rev Immunol. 2005;23:225-274.
26. Haedicke W, Ho FC, Chott A, et al. Expression of CD94/NKG2A and killer immunoglobulin-like receptors in NK cells and a subset of extranodal cytotoxic T-cell lymphomas. Blood. 2000;95: 3628-3630.
27. Morice WG, Macon WR, Dogan A, Hanson CA, Kurtin PJ. NK-cell-associated receptor expression in hepatosplenic T-cell lymphoma, insights into pathogenesis. Leukemia. 2006;20:883-886.
28. Kim DK, Kabat J, Borrego F, Sanni TB, You CH, Coligan JE. Human NKG2F is expressed and can associate with DAP12. Mol Immunol. 2004;41: 53-62.

Cell Host & Microbe
Article

Host Cell Traversal Is Important for Progression of the Malaria Parasite through the Dermis to the Liver

Rogerio Amino,[1,2,6] Donatella Giovannini,[1,6] Sabine Thiberge,[1] Pascale Gueirard,[1] Bertrand Boisson,[1] Jean-François Dubremetz,[3] Marie-Christine Prévost,[4] Tomoko Ishino,[1,5] Masao Yuda,[5] and Robert Ménard[1,*]
[1]Unité de Biologie et Génétique du Paludisme, Institut Pasteur, 28 Rue du Dr Roux, 75724 Paris cedex 15, France
[2]Departamento de Bioquimica, Universidade Federal de Sao Paulo, Rua Três de Maio 100, 04044-020, Sao Paulo, Brazil
[3]UMR 5539 CNRS, Université de Montpellier 2, Place Eugène Bataillon, 34095 Montpellier cedex 05, France
[4]Plate-forme de microscopie électronique, Institut Pasteur, 25-28 rue du Dr Roux, 75724 Paris cedex 15, France
[5]Mie University, School of Medicine, 2–174 Edobashi, Tsu, Mie 514-0001, Japan
[6]These authors contributed equally to this work.
*Correspondence: rmenard@pasteur.fr
DOI 10.1016/j.chom.2007.12.007

SUMMARY

The malaria sporozoite, the parasite stage transmitted by the mosquito, is delivered into the dermis and differentiates in the liver. Motile sporozoites can invade host cells by disrupting their plasma membrane and migrating through them (termed cell traversal), or by forming a parasite-cell junction and settling inside an intracellular vacuole (termed cell infection). Traversal of liver cells, observed for sporozoites in vivo, is thought to activate the sporozoite for infection of a final hepatocyte. Here, using *Plasmodium berghei*, we show that cell traversal is important in the host dermis for preventing sporozoite destruction by phagocytes and arrest by nonphagocytic cells. We also show that cell infection is a pathway that is masked, rather than activated, by cell traversal. We propose that the cell traversal activity of the sporozoite must be turned on for progression to the liver parenchyma, where it must be switched off for infection of a final hepatocyte.

INTRODUCTION

Malaria infection is initiated when an *Anopheles* mosquito injects *Plasmodium* sporozoites into the dermis of the host (Sidjanski and Vanderberg, 1997; Matsuoka et al., 2002; Vanderberg and Frevert, 2004; Amino et al., 2006; Yamauchi et al., 2007). Sporozoites travel from the site of mosquito bite to the liver, where they enter and settle inside hepatocytes. They then multiply and differentiate into the parasite form called merozoite, which infects red blood cells and causes the symptoms of the disease.

The journey and fate of the sporozoite in the mammalian host is still a poorly documented part of the parasite life cycle. A recent quantitative in vivo imaging study has revealed that sporozoites inoculated by a mosquito reach not only the liver, via the bloodstream, but also the lymph node draining the site of the mosquito bite, where most are internalized inside dendritic cells and some can initiate development (Amino et al., 2006). In liver sinusoids, sporozoites interact with resident macrophages, the Kupffer cells, which are thought to act as necessary gates to the underlying parenchyma (Pradel and Frevert, 2001; Frevert et al., 2005; Baer et al., 2007).

The elongated sporozoite cell displays an active gliding locomotion on solid substrates in vitro and in host tissues, reaching speeds up to 4 μm/s, which is powered by a submembranous actin-myosin motor (Ménard, 2001; Kappe et al., 2004). Using this motor, the sporozoite can invade host cells in two distinct ways. Like other invasive stages of Apicomplexa protozoa, it can penetrate the cell inside a so-called parasitophorous vacuole (PV) formed by invagination of the host cell plasma membrane. Typically, the apicomplexan zoite forms an intimate junction between its anterior pole and the contacting host cell surface, the so-called moving junction (MJ), on which it must exert force to pull itself inside the nascent vacuole (Hollingdale et al., 1981; Sibley, 2004). This process, termed here cell infection, is a prerequisite for complete sporozoite differentiation into merozoites and occurs in vivo inside hepatocytes.

The sporozoite can also disrupt host membranes and migrate through and out of the cell. The cell traversal behavior of the sporozoite was first described with macrophages (Vanderberg et al., 1990) and later shown to also occur with epithelial cells and fibroblasts (Mota et al., 2001). In the *P. berghei* species that infect rodents, this activity was documented in vivo only in the liver (Frevert et al., 2005; Mota et al., 2001). Based on work performed with *P. berghei*-hepatocyte in vitro systems, the current view is that, in vivo, sporozoites traverse several hepatocytes before infecting a final hepatocyte, and that the former step has a dual activating role on the latter. First, it appeared to render the sporozoite competent for infecting a final cell inside a PV, by inducing progressive exocytosis of the parasite proteins specifically involved in this process (Mota et al., 2002). Second, it was found to cause the release of hepatocyte growth factor (HGF) from traversed cells, and HGF to promote parasite development in infected cells via cMET-dependent signaling pathways (Carrolo et al., 2003).

More recent work, however, has challenged these conclusions. Inactivation in *P. berghei* of the genes named *spect* (Ishino

et al., 2004) or *spect2* (Ishino et al., 2005a) impaired the sporozoite capacity to traverse hepatoma cells lines without affecting its ability to develop inside these cells. Host cell traversal was found to be important for sporozoite crossing the liver sinusoid barrier, possibly by migrating through Kupffer cells (Ishino et al., 2004, 2005a). SPECT and SPECT2 are structurally unrelated secretory proteins, and SPECT2 possesses a typical membrane-attack/perforin (MACPF)-like domain, found in pore-forming proteins such as components of the mammalian complement system and perforin.

Here, to further study the role of host cell traversal in vivo, we rendered *spect(–)* and *spect2(–)* sporozoites fluorescent and characterized their behavior by real-time imaging both in vivo and in vitro.

RESULTS

Generation and Cell Traversal Activity of the ConF, SpectF, and Spect2F Sporozoites

We first generated a fluorescent *P. berghei* ANKA clone, named ConF, by integrating at the *DHFR-TS* locus of the wild-type the *GFP* gene fused to *HSP70* regulatory sequences (see Figure S1 available online). Erythrocytic stages of the *P. berghei spect(–)* and *spect2(–)* clones (Ishino et al., 2004, 2005a) were separately mixed with erythrocytic stages of the ConF clone and transmitted to *Anopheles stephensi* mosquitoes, where meiosis and random chromosome segregation occur. The double transgenic parasites *spect–/gfp+* and *spect2–/gfp+* emerging from cross-fertilized zygotes, named SpectF and Spect2F, respectively, were cloned as erythrocytic stages after parasite cycling (Figure S1).

The ConF, SpectF, and Spect2F clones were then transmitted to *Anopheles stephensi* mosquitoes, and 18 days after parasite transmission, similar numbers of sporozoites in the three clones were present in the mosquito salivary glands. In matrigel, ~80% of the sporozoites in the three clones glided with an average velocity of ~1.4 μm/s for up to 30 min at 37°C (Figure 1A and Figure S2), typically following a corkscrew path while occasionally moving randomly. To examine sporozoite capacity to wound host cell plasma membranes, sporozoites were recorded for 30 min inside matrigels containing host cells in the presence of SYTOX Orange, a nucleic acid stain that penetrates cells with compromised plasma membranes and fluoresces in the nucleus. Cells fluorescent after 30 min were individually examined and scored as wounding events when cell fluorescence started less than 2 min after sporozoite contact. ConF sporozoites wounded all cell types tested, i.e., mast cells and dermal fibroblasts (data not shown), primary hepatocytes (Figure 1B), and HepG2 hepatoma cells (Figure 1C and Movie S1). In primary hepatocytes, ConF sporozoites (multiplicity of infection = 1) provoked an average of 1.8 wounding events/sporozoite/hr. In contrast, SpectF and Spect2F sporozoites did not induce host cell fluorescence in any of the cell types tested. The *spect* and *spect2* genes are thus both dispensable for sporozoite gliding in three-dimensional (3D) matrices but individually critical for the membrane-damaging capacity of the sporozoite.

Host Cell Traversal Is Important in the Dermis of the Host

To test whether the traversal activity was important during the skin phase of the sporozoite's journey, we compared infectivity of intravenously or subcutaneously injected wild-type or *spect(–)* sporozoites in animals treated with liposome-encapsulated clodronate. Clodronate destroys macrophages in the liver and, to a lesser extent, in the spleen, but not in other tissues (van Rooijen et al., 1997). In these animals, intravenously injected wild-type and mutant sporozoites had similar infectivity, whereas subcutaneously injected mutant sporozoites were ~5- to 10-fold less infective than the wild-type (Figure 2A). This suggested that the traversal activity was important during the sporozoite transit in the skin.

We then examined by intravital imaging the fate of sporozoites in the dermis of mice after natural transmission. A single mosquito was allowed to probe the ear of an anesthetized Hairless mouse for 1 min, and the probed site was observed by spinning disk confocal microscopy (Amino et al., 2007) at various times postinfection (p.i.). Like *P. berghei* NK65 sporozoites (Amino et al., 2006), most (~80%) ANKA ConF sporozoites glided at an average speed of ~1–2 μm/s, following a tortuous path (Figures 2B and 2C; Figure S3). In contrast, most mutant sporozoites were immotile, with only ~10% of the sporozoites in the two mutant clones gliding between 15 and 30 min p.i. (Figures 2B and 2C; Figure S3). In agreement with their normal gliding in 3D matrices, the path and speed of the few mutant sporozoites that were motile were similar to those of ConF sporozoites. Therefore, most of the mutants, despite normally gliding in 3D matrices, were rapidly immobilized in the dermis, presumably by host cells they cannot traverse.

Host Cell Traversal Is Important for Resisting Clearance by Phagocytes in the Dermis

We next tested whether host leukocytes were involved in the arrest of cell traversal-deficient mutants in the dermis. Spect2F sporozoites were transmitted to Hairless mice by mosquito bite, and the site of bite was extracted, stained with antibodies to CD11b, a leukocyte-specific antigen, and examined by confocal microscopy. At 5 and 30 min p.i., when ~75% of the control sporozoites are motile, about 10% and 50% of the mutant sporozoites, respectively, were associated with CD11b+ cells (Figure 3A), and ~25% of the mutants could be detected inside these cells after 30 min (Figure 3B). Similar results were obtained using SpectF sporozoites (data not shown).

Interactions between SpectF sporozoites and host phagocytes were then imaged in real-time in *lys-gfp* mice (Faust et al., 2000), in which myelomonocytic cells (macrophages, neutrophil granulocytes, and dendritic leuykocytes) express GFP (Figures 3C and 3D). At the mosquito bite sites, weakly fluorescent, resident phagocytes were present, while brightly fluorescent cells were recruited starting at ~25 min p.i. (Figure 3C). Mutant sporozoites were rapidly immobilized, as early as 3 min p.i., and were frequently seen in contact with dermal cells, labeled by red fluorescent BSA, or green fluorescent phagocytic cells. The fluorescence of many mutant sporozoites gradually faded during 1 hr observation periods (Figure 3D, blue inset). Importantly, however, although cell traversal-deficient sporozoites could be destroyed by phagocytic cells, the fluorescence of some sporozoites remained unchanged with time (Figure 3D, red inset), suggesting that immobilized mutants could also escape degradation.

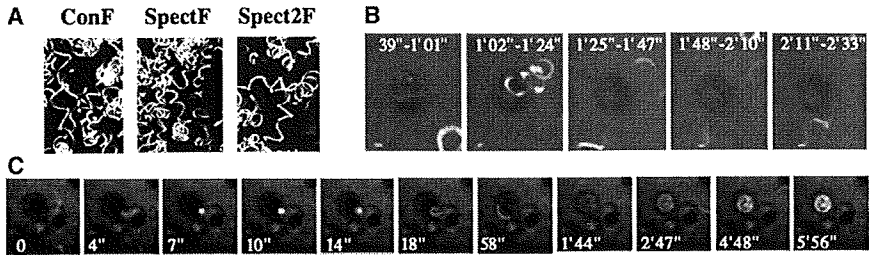

Figure 1. Sporozoite Gliding Motility and Cell Traversal Ability

(A) Sporozoite motility in matrigel. Sporozoites were mixed with matrigel and were imaged in multiple z layers for 5 min. The path of sporozoites is represented by the maximum intensity projection of the fluorescent signal.

(B and C) Time-lapse microscopy of a ConF sporozoite traversing a primary hepatocyte (B) or a HepG2 hepatoma cell (C) in the presence of SYTOX Orange. Sequential images are shown as maximum intensity projections of the fluorescence signal recorded during the time intervals (B) or time points (C) indicated. Each Z plane, acquired using the 488 nm (GFP) and the 568 nm (SYTOX) channels, was projected over time and pseudocolored: Z4 (depth of 40 μm) in red, Z5 (depth of 50 μm) in green, and Z6 (depth of 60 μm) in blue.

Cell Traversal-Deficient Sporozoites Are Arrested by and Readily Invade Dermal Fibroblasts

The fact that a proportion of mutant sporozoites immobilized in the dermis were not associated with CD11b+ cells and were not destroyed by phagocytes suggested that mutants might also invade nonprofessional phagocytes. To test this, we examined sporozoite interactions with fibroblasts, a major nonphagocytic cell type in the dermis. ConF, SpectF, or Spect2F sporozoites were mixed with either human foreskin fibroblasts (HFF) or mouse dermal fibroblasts (ATCC CRL-2017) in matrigel, the trajectories of gliding sporozoites were visualized as maximal intensity projections, and the proportion of immotile sporozoites was counted at various times (Figures 4A–4D). For up to 30 min, ~80% of the ConF sporozoites moved in a pattern indistinguishable from that in cell-free matrigel, showing that the presence of host cells did not affect motility of normal sporozoites. In contrast, less than 20% of the sporozoites in both mutant clones were still motile after 30 min (Figures 4C and 4D), most mutant sporozoites being immobilized in association with a cell (Figure 4B). Time-lapse imaging showed that mutant sporozoites were suddenly arrested upon the first contact with a fibroblast, frequently remaining bound to the host cell surface for extended periods of time (Figure 4E and Movie S2). To test whether mutant sporozoites could penetrate fibroblasts, SpectF sporozoites were incubated with HFF cells, and after 30 min thin sections were examined by transmission electron microscopy (TEM). SpectF sporozoites were detected inside cells and surrounded by a membrane (Figure 4F), showing that mutant sporozoites could also be arrested by and invade dermal fibroblasts.

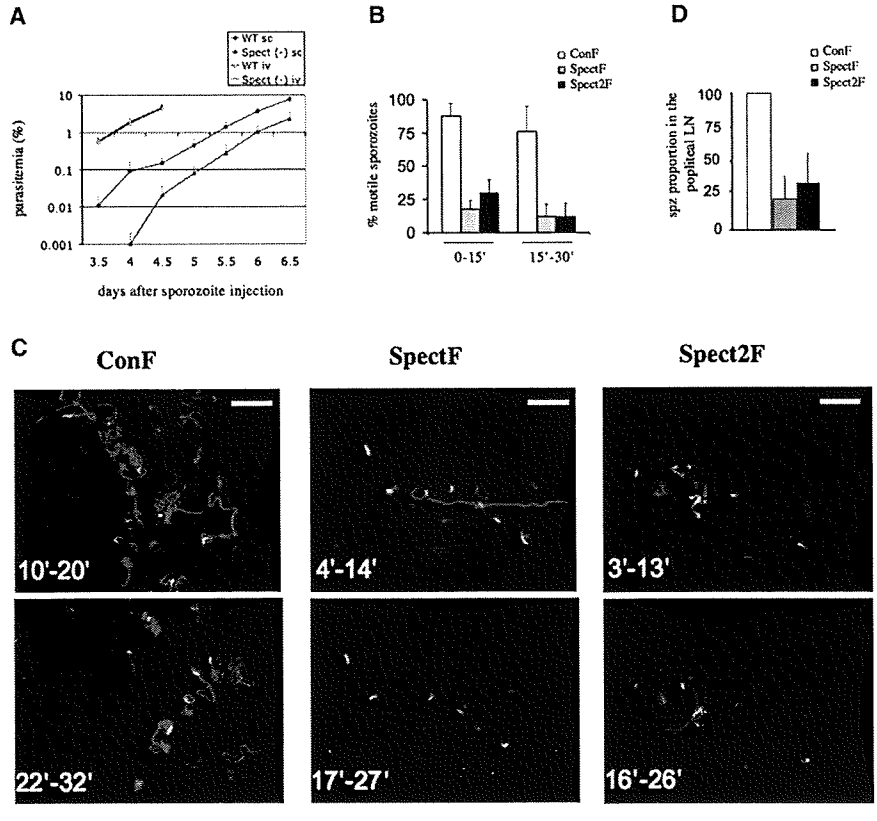

Figure 2. Host Cell Traversal Is Important in the Skin

(A) Infectivity of wild-type and *spect(–)* sporozoites injected intravenously (iv; 30,000) or subcutaneously (sc; 50,000) in clodronate treated rats (n > 5 animals). The graph shows the average + SD of the parasitemia in logarithmic scale.

(B and C) Motility of sporozoites injected by a mosquito into the ear of a Hairless mouse. (B) Percentage of motile parasites during the first 15 min and between 15 and 30 min after the bite. The bar represents the average + SD in 10 min of analysis (n = 3–6 bites). Numbers of sporozoites analyzed: ConF = 174, SpectF = 157, Spect2F = 195. (C) Maximum intensity projections of the fluorescent signal (in red) of sporozoites gliding during the indicated period of time. Scale bar, 50 μm.

(D) Proportion of cell traversal-deficient mutants that reach the politeal lymph node (LN) 2 hr after infection compared to the wild-type (n = 5 animals). The bars represent the average + SD of five experiments for each mutant.

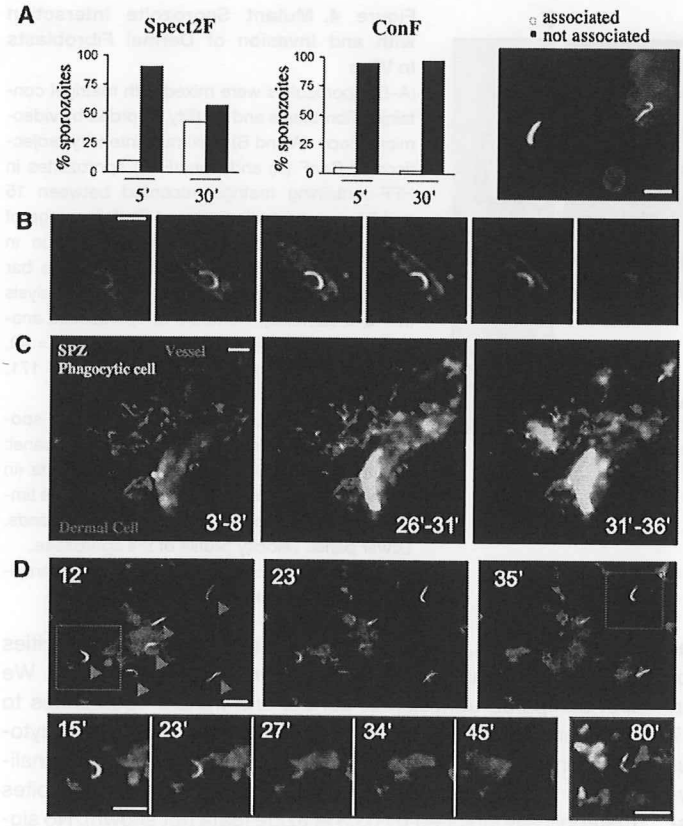

Figure 3. Mutant Sporozoite Interactions with Host Leukocytes

(A and B) Spect2F and ConF interaction with CD11b+ cells in Hairless mice. A mouse was bitten by Spect2F- or ConF- infected mosquitoes in the abdomen, and the bite site was extracted, fixed with 4% paraformaldehyde/PBS, stained with rat anti-mouse CD11b-Alexa 647 mAb, and analyzed by confocal microscopy. Scale bars, 15 μm. (A) Percentage of Spect2F or ConfF sporozoites associated or not with CD11b+ cells 5 and 30 min after the bite (86 Spect2F and 49 ConF sporozoites analyzed). Similar results were obtained using SpectF sporozoites (n = 51). (B) A SpectF sporozoite inside a CD11b+ cell in the dermis. The panel shows 6 z stacks (z step, 1 μm) recorded sequentially with a double wavelength excitation of 488 nm (GFP) and 647 nm (CD11b). The centrality of the sporozoite within the panel of z stacks confirms its intracellular localization. (C and D) Fate of SpectF sporozoites in the dermis of the ear of *lys-gfp* mice.

(C) Time-lapse microscopy of leukocyte recruitment at the sporozoite-containing site in the dermis. Dermal cells, which take up red-fluorescent BSA injected intravenously into the animal prior to imaging, are labeled in red, and the blood vessel is represented in blue. A massive recruitment of brightly fluorescent cells is seen starting at ~25 min p.i. that progressively infiltrate the sporozoite-containing site. Scale bar, 30 μm.

(D) Time-lapse microscopy of the fate of six dermal SpectF sporozoites. The upper panel (three images) follows the six sporozoites over time: three (indicated by blue arrowheads) no longer fluoresce after 35 min, while three others (indicated by red arrowheads) still fluoresce after that time. The lower left time-lapse view (five images) shows the progressive degradation of the leftmost sporozoite of the upper panel (blue-squared). The lower right image shows the red-squared sporozoite of the upper panel that still fluoresces after 80 min. Scale bars, 15 μm.

Host Cell Traversal Is Not Essential for Crossing Endothelial Barriers in the Dermis

Next, we tested whether host cell traversal played a role during sporozoite crossing endothelial barriers in the dermis. We have shown that sporozoites can actively cross the walls of both blood and lymphatic vessels in the dermis, and that ~1% of the *P. berghei* NK65 sporozoites inoculated in the mouse footpad by subcutaneous injection terminate their journey and accumulate in the first draining (popliteal) lymph node (Amino et al., 2006). Similarly, after injection of 10^4 ConF sporozoites in the footpad of mice, an average of ~1%–2% was counted in the popliteal node after 2 hr. To compare the capacity of mutant and control sporozoites to reach the popliteal node, we injected the same number of SpectF or Spect2F sporozoites in the footpad of a mouse and of ConF sporozoites contralaterally and counted the number of sporozoites in the popliteal nodes 2 hr p.i. (Figure 2D). The numbers of SpectF and Spect2F sporozoites were only 25% and 32% of that of ConF sporozoites, respectively. The similar decrease in the proportion of mutant sporozoites in the lymph node at 2 hr p.i. (Figure 2D) and in the proportion that initially glided in the dermis (Figure 2B) thus suggests that mutant sporozoites have no specific defect in crossing the wall of lymph vessels. The residual infectivity of mutant sporozoites delivered to normal rats by mosquito bite (data not shown) or injected subcutaneously in normal (data not shown) or clodronate-treated animals (Figure 2A) also indicates that cell traversal is not essential for crossing the wall of dermal blood vessels. Therefore, immobilization of mutant sporozoites inside leukocytes or other cell types in the dermis seems to constitute a primary defect, rather than a consequence of an inability to cross endothelial barriers in the dermis.

Cell Traversal Retards, Rather Than Activates, Hepatocyte Infection

We next investigated sporozoite traversal of hepatocytes. Previous studies have suggested that sporozoites traverse several hepatocytes in vivo before final infection (Frevert et al., 2005; Mota et al., 2001). In agreement with this, ConF sporozoites were found to glide extensively in the liver parenchyma before finally arresting, as exemplified in Figure S4 (Movie S4). To study cell traversal in the liver parenchyma, we first compared the differentiation of ConF, SpectF, and Spect2F sporozoites in rodent primary hepatocytes. *P. berghei* sporozoites develop into exoerythrocytic forms (EEF) that yield after ~60 hr thousands of mature merozoites, the erythrocyte-infecting stage (Sturm et al., 2006). No difference was noticed between the three clones in the number, size, and fluorescence intensity of EEF at 4, 12, 24, or 48 hr in rat (Figure 5A) or mouse (data not shown) primary hepatocytes. The three clones generated merozoites with similar infectivity to rats, as measured by prepatent periods of infection (data not shown). Therefore parasite development inside hepatocytes does not appear to depend on prior traversal of these cells.

To examine sporozoite entry into primary hepatocytes, infection events (parasites internalized inside a vacuole) were measured after 1 hr incubation, when sporozoites are no longer motile and invasive. For this, samples fixed at 1 hr were labeled with antibodies to the sporozoite CS surface protein to discriminate extracellular (red) from intracellular (green) parasites, and infection

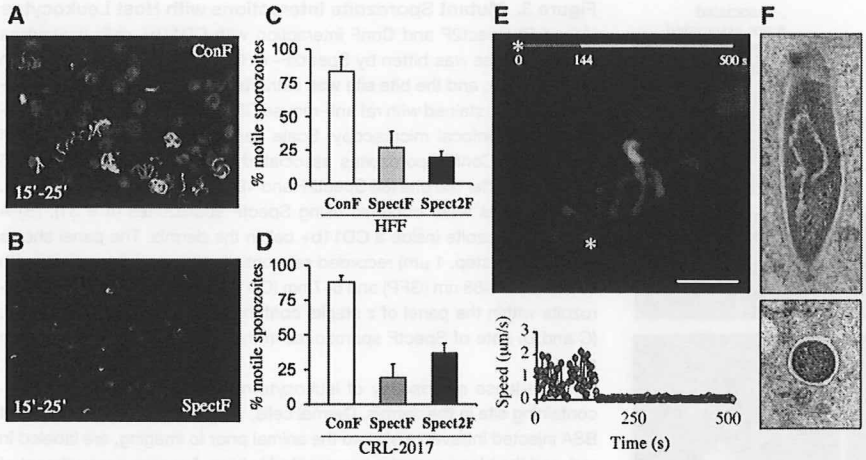

Figure 4. Mutant Sporozoite Interaction with and Invasion of Dermal Fibroblasts In Vitro

(A–D) Sporozoites were mixed with matrigel containing fibroblasts and motility recorded by videomicroscopy. (A and B) Maximum intensity projections of ConF (A) and SpectF (B) sporozoites in HFF-containing matrigel recorded between 15 and 25 min incubation. (C and D) Percentage of motile sporozoites after 10 min incubation in HFF- or CRL-2017-containing matrigel. The bar represents the average ± SD in 10 min of analysis (n = 3–6 samples). Numbers of sporozoites analyzed using HFF cells: ConF = 110, SpectF = 40, Spect2F = 99; using CRL-2017 cells: ConF = 171, SpectF = 86, Spect2F = 175.

(E) Immobilization of a representative SpectF sporozoite upon contact with a HFF cell. Upper panel: maximum intensity projection of the parasite (in red before the initial contact, green after). The timing of the color code is indicated in seconds. Lower panel: velocity profile of the sporozoite.

(F) TEM pictures of SpectF sporozoites internalized in HFF cells after 30 min incubation.

events counted as green parasites (see Experimental Procedures). After 1 hr incubation with primary hepatocytes, ~20% of the initial sporozoites in the three clones were scored as infection events (Figure 5B). Similar results were obtained using CRL-2017 dermal fibroblasts (Figure 5B). The kinetics of cell invasion by mutant and control sporozoites were then compared by TEM analysis of primary hepatocytes fixed after 10 or 30 min incubation. Using Spect2F sporozoites, at both 10 and 30 min a high proportion of cells (37%) contained an intracellular parasite, and as expected, 100% of the intracellular Spect2F sporozoites were surrounded by a membrane (Figure 5C and Figure S5). Instead, using ConF sporozoites, a lower proportion of cells (~15%) contained an intracellular parasite, and the proportion of intracellular parasites surrounded by a membrane increased from 35% to 60% after 10 and 30 min, respectively (Figure 5C and Figure S5).

The rapid kinetics of hepatocyte invasion by mutant sporozoites was confirmed by CS staining assays (Figures 6A and 6B). Using Spect2F, the first intracellular sporozoites were detected after only 2 min incubation, >2% of the sporozoites appeared bicolor (half red/CS-half green/GFP) during the first 4 min, presumably fixed during cell penetration, and the final levels of 20% of internalized sporozoites were reached after only 10 min. Similar results were obtained during entry of Spect2F sporozoites into dermal fibroblasts (Figure S6) and with SpectF sporozoites in both cell types (data not shown). Time-lapse imaging of Spect2F sporozoites incubated with primary hepatocytes readily showed sporozoites displaying and moving through a constriction, suggestive of a MJ, at the site of host cell contact (Figure 6C and Movie S3). Finally, TEM analysis of samples fixed at 3 min detected Spect2F sporozoites entering primary hepatocytes while forming a MJ with the host cell surface (Figure 6D), which is seen here for the first time between a *Plasmodium* sporozoite and a mammalian cell.

Constitutive Infection by Mutant Sporozoites Is Due to Lack of Cell Traversal

Finally, we addressed the possibility that the "rapid invader" phenotype of the mutants might be due to secondary changes on their surfaces, conferring gain-of-function infective capacities that would normally be activated by traversal of host cells. We first compared adhesion of control and mutant sporozoites to confluent CRL-2017 monolayers in the presence of 1 µg/ml cytochalasin (Figures 7A and 7B), which prevents parasite internalization into but not attachment to host cells, or using sporozoites metabolically inhibited by 0.03% azide (data not shown). No significant difference between adhesion of control and mutant sporozoites to cells was noticed in any of these conditions. Also, using real-time qPCR, we compared in salivary gland sporozoites the levels of transcripts encoding the 13 parasite products currently known or suspected to be involved in sporozoite adhesion and/or invasion of host cells, listed in Figure 7C. No significant difference was observed in expression of any of these genes in ConF, SpectF, and Spect2F sporozoites (Figure 7C). These data confirm the view that the "rapid invader" phenotype of the mutants is a direct consequence of their lack of cell traversal.

DISCUSSION

The primary function of the host cell traversal capacity of the *Plasmodium* sporozoite, first described by Vanderberg and collaborators in 1990, remains controversial. Because the traversal activity in vivo was documented first in hepatocytes in rodents, it was presumed that traversing hepatocytes was an important step that would directly favor the final infection step in a PV (Mota et al., 2001). In vitro data have suggested that traversal of hepatocytes was essential in two distinct ways: by rendering the sporozoite competent for entering a cell inside a PV (Mota et al., 2002) and by modifying the infected hepatocyte for optimal development of he parasite in the PV (Carrolo et al., 2003). The results presented here, along with previous studies (Ishino et al., 2004, 2005a), suggest a different contribution of the cell traversal activity.

We show here that this activity is first important in the dermis of the host, where it primarily prevents sporozoite destruction by phagocytic cells. A secondary effect of cell traversal might be to avoid infection of cells that sporozoites can penetrate inside

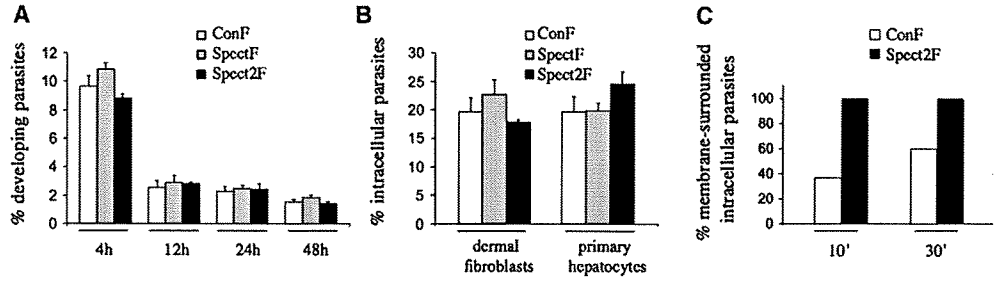

Figure 5. The Cell Traversal-Deficient Mutants Infect Primary Hepatocytes at Normal Levels and Normally Develop inside These Cells

(A) Percentage of parasites developing inside rat primary hepatocytes. Salivary gland sporozoites (15×10^4) were added to nonconfluent cells (multiplicity of infection = 1), and maturing parasites were counted in the entire well by fluorescence microscopy after various incubation times at 37°C. (B) Percentage of sporozoites internalized in CRL-2017 dermal fibroblasts and rat primary hepatocytes after 1 hr incubation. Infections were initiated as in (A), samples were labeled with anti-CS antibody after 1 hr, and the proportion of intracellular parasites counted by fluorescence microscopy as green parasites. The bars in (A) and (B) represent the average + SD of three independent experiments each performed in triplicate. (C) Percentage of intracellular parasites surrounded by a vacuolar membrane in rat primary hepatocytes. Infections were processed for TEM after 10 or 30 min incubation, and 159 ConF (in 620 cells) and 111 Spect2F (in 269 cells) intracellular parasites were counted.

a vacuole but are not their final destination, such as dermal fibroblasts. These two roles might serve the sporozoite at other steps of its journey to the liver parenchyma, including, as previously suggested, for resistance to clearance by Kupffer cells in liver sinusoids (Ishino et al., 2004, 2005a). We found no evidence, however, that cell traversal is important for crossing endothelial barriers in the dermis, and whether it is required for crossing the endothelium of liver sinusoids is still debated. Clodronate, which kills Kupffer cells, restores infectivity of the intravenously injected mutant sporozoites. This would suggest a role of cell traversal in resisting killing by Kupffer cells, but clodronate treatment might also create gaps in the liver sinusoidal barrier and thus artificial gates to the parenchyma (Baer et al., 2007). Therefore, cell traversal appears to be important in at least two steps of the sporozoite's journey: in the dermis, for freely moving until endothelial barriers are reached and for resisting attacks by phagocytic cells in the process, and in the liver sinusoids, presumably for resisting destruction by Kupffer cells.

The interactions between the cell traversal-deficient mutants and primary hepatocytes described here are irreconcilable with the currently accepted model of the role played by hepatocyte traversal in the sporozoite's life (Mota and Rodriguez, 2004; Leiriao et al., 2004; Waters et al., 2005; Prudencio et al., 2006). First, the normal differentiation of cell traversal-deficient parasites inside hepatocytes, as well as in vivo in the absence of Kupffer cells (Ishino et al., 2004, 2005a), demonstrates that parasite development does not depend on any factor released by wounded cells acting on infected cells. Second, the kinetics of cell infection by sporozoites, observed using both primary hepatocytes and dermal fibroblasts, clearly suggests that prior cell traversal retards, rather than activates, the final cell infection step. We found that mutant and control sporozoites only differed by the lack of cell traversal and a rapid/synchronized cell infection in the former, suggesting that lack of cell traversal directly causes (and might be sufficient for) the rapid invader phenotype. Therefore, the cell infection pathway unmasked by the lack of cell traversal in the mutants should also be constitutively available in the normal sporozoite. Successful cell infection by the normal sporozoite might only necessitate turning off the antagonistic cell traversal activity.

In this view, sporozoite entry inside a PV would require formation of the MJ and the PV as well as silencing of the cell traversal activity. The MJ and PV biogenesis, which clearly do not depend on prior cell traversal, might be triggered by host cell contact.

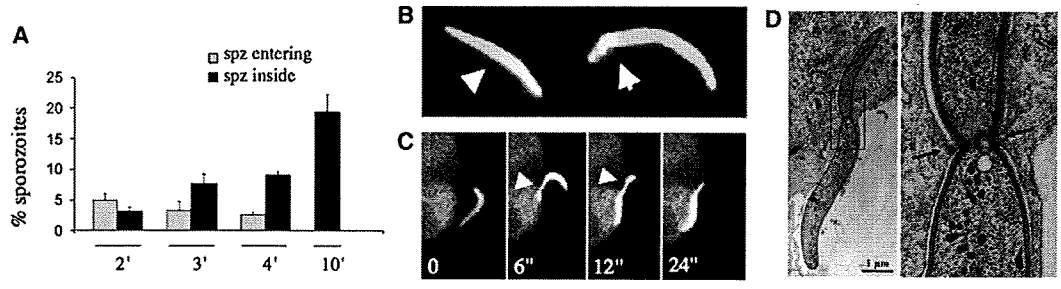

Figure 6. The Cell Traversal-Deficient Mutants Rapidly Invade Host Cells by Forming a Moving Junction

(A) Percentage of Spect2F sporozoites entering or fully internalized in rat primary hepatocytes during the first 10 min incubation. Infections were initiated as in Figure 5A, samples were labeled with anti-CS antibody after the various incubation times, and entering and intracellular sporozoites were scored as bicolor and green parasites, respectively. The bars represent the average + SD of three independent experiments each performed in triplicate.

(B) Representative merged pictures of entering, bicolor Spect2F sporozoites. The arrowheads indicate the junction between the extracellular (yellow) and intracellular (green) portions of the parasites.

(C) Time-lapse microscopy of a Spect2F sporozoite interacting with a primary hepatocyte in matrigel. Arrowheads point to the parasite constriction at the site of host cell contact. The time (in seconds) is indicated.

(D) TEM pictures of a Spect2F sporozoite entering a rat primary hepatocyte and zoom-in (right panel) on the host-parasite moving junction.

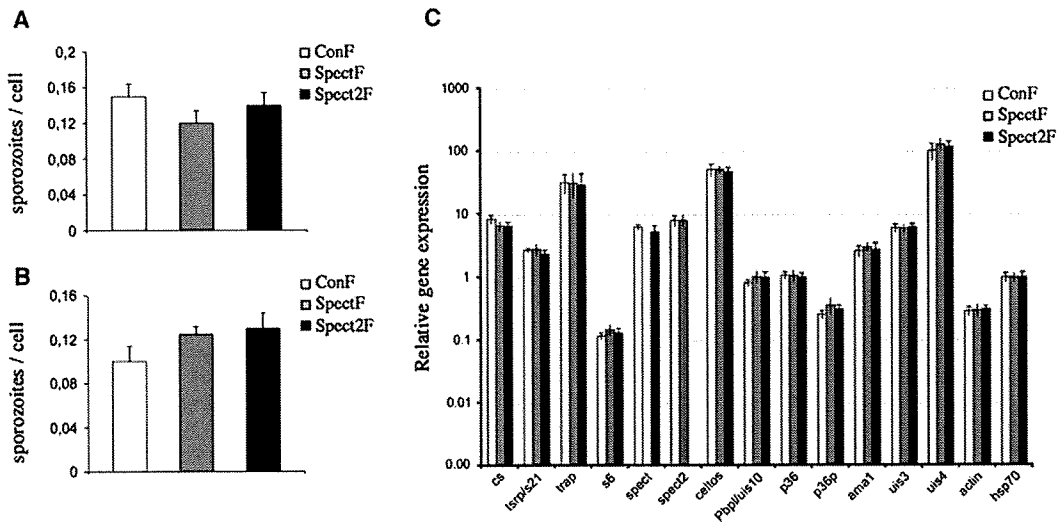

Figure 7. The Cell Traversal-Deficient Mutants Normally Adhere to Host Cells and Express Normal Levels of Adhesion/Invasion-Related Transcripts

(A and B) Confluent monolayers of murine CRL-2017 fibroblasts were incubated with 1.5 x 10^4 salivary gland sporozoites in the presence of 1 μg/ml cytochalasin D, samples were not centrifuged (A) or centrifuged for 1 min at 4°C at 800 rpm to facilitate parasite-host cell interactions (B), and after 15 min incubation at 37°C the numbers of attached sporozoites per cell were counted. The bars represent the average + SD of triplicates.

(C) Histogram representation of qPCR analysis of gene expression in ConF, SpectF, and Spect2F sporozoites collected from salivary glands of mosquitoes at day 21 of infection. The genes tested are *CS* (Sinnis et al., 1994), *TRSP* (Labaied et al., 2007), *TRAP* (Sultan et al., 1997), S6 (Kaiser et al., 2004), *spect* (Ishino et al., 2004), *spect2* (Ishino et al., 2005a), *CelTOS* (Kariu et al., 2006), *Pbpl/uis10* (Bhanot et al., 2005), *P36* and *P36p* (Ishino et al., 2005b; van Dijk et al., 2005), *AMA1* (Silvie et al., 2004), and *UIS3* and *UIS4* (Mueller et al., 2005a, 2005b). Mean values were obtained from three independent batches of sporozoites of each clone. x axis: genes tested; y axis: log scale of mean normalized expression (hsp70). Standard deviations for all genes tested were 20%–30% of gene expression, except for *TRAP* using Spect2F sporozoites (50%).

Recently, a study found that the sporozoite uses the sulfation level of heparan sulfate proteoglycans (HSPGs) on the surface of host cells as a Global Positioning System (Coppi et al., 2007). Sporozoites continue to migrate through cells expressing undersulfated HSPG and to switch to invasion in a PV into cells covered with highly sulfated HSPG, primarily hepatocytes. However, whether the cell surface sulfated signal acts to promote the formation of the MJ and PV or to silence cell traversal, or both, remains unknown. Theoretically, cessation of the cell traversal activity might be time dependent or induced upon contact with the target cell (possibly with HSPGs) or by cell traversal itself.

How cell traversal is achieved is also unclear. Sporozoites might directly rupture the host cell plasma membrane upon contact with the parasite, or initially enter inside the cell via a MJ and immediately escape from the vacuole. The former view would fit with the initial description of *P. berghei* sporozoites entering and exiting rodent peritoneal macrophages in a "needling manner and inducing an outward flow of host cell cytoplasm at the point of egress" (Vanderberg et al., 1990). The latter scenario would be reminiscent of the way sporozoites cross acinar cells of the mosquito salivary glands to reach the secretory cavities, i.e., by entering cells through the formation of a MJ while concomitantly lysing the membrane of the nascent PV (Pimenta et al., 1994).

In conclusion, the data presented here suggest that the host cell traversal activity ensures progression of the *Plasmodium* sporozoite from the site of mosquito bite to the liver parenchyma, where its repression allows final infection of a hepatocyte. One important function associated with the cell traversal activity is the resistance to killing by host phagocytic leukocytes, but how this is achieved awaits further characterization. The picture that emerges from this and previous intravital imaging studies of the *Plasmodium* sporozoite in rodent hosts (Vanderberg and Frevert, 2004; Amino et al., 2006, 2007) is that the *Plasmodium* sporozoite relies on two robust abilities, host cell traversal and extracellular gliding, to reach its final niche in the liver. This contrasts with the strategy of the other well-studied and closely related Apicomplexan parasite, the *Toxoplasma* tachyzoite, which lacks cell traversal activity and hijacks host motile leukocytes for delivery to destination (Courret et al., 2006; Lambert et al., 2006).

EXPERIMENTAL PROCEDURES

Mosquitoes

Anopheles stephensi (Sda500 strain) mosquitoes were reared at the Centre for Production and Infection of *Anopheles* (CEPIA) at the Pasteur Institute using standard procedures. Mosquitoes were fed on infected mice 3–5 days after emergence and kept as already described (Amino et al., 2006, 2007). Infected mosquitoes used for transmission experiments (days 18–22 after the infectious blood meal) were deprived of sucrose for 1–2 days before experimentation to enhance the mosquito bite rate. For in vitro experiments, sporozoites were isolated from infected salivary glands 18–22 days after the infectious blood meal and kept on ice in tissue culture medium with 10% fetal calf serum (FCS).

Mice Manipulation

All experiments using rodents were approved by the committee of the Pasteur Institute and were performed in accordance with the applicable guidelines and regulations. For sporozoite analysis in lymph nodes, 10^4 salivary gland sporozoites in 3 μl PBS were microinjected in the right (in the case of ConF sporozoites) and in the left (in the case of SpectF or Spect2F sporozoites) footpad. The popliteal lymph node was removed by minimally invasive surgery after 2 hr.

Microscopy and Image Analysis

Microscopic analysis was carried out using a high-speed spinning disk confocal system (Ultraview ERS, Perkin Elmer) mounted on an inverted Axiovert 200 microscope (Carl Zeiss) with Optovar option linked to a Orca II ER camera (Hamamatsu, Japan). Image files were processed using ImageJ. Sporozoites in the dermis of mice were imaged as already described (Amino et al., 2007).

Primary Hepatocytes

Rat (4-week-old female Wistar) and mouse (6- to 8-week-old female C57BL/6) hepatocytes (Janvier, France) were isolated from animals treated with sodium pentobarbital by a modified two-step collagenase perfusion method. Briefly, the liver was perfused via the portal vein for 10 min with liver perfusion medium 1× (GIBCO 17701) followed by a 10 min perfusion with liver digest medium 1× (GIBCO 17703) at a flow rate of 6–10 ml/min. Isolated cells were washed and centrifuged through a Percoll gradient to remove damaged cells. Cell viability (>90%) was determined by trypan blue exclusion. Hepatocytes were plated at a density of 6–15 × 10^4 in 8-well permanox Lab-Tek chamber slides in Williams medium E containing 10% FCS. Cells were maintained at 37°C in a humidified atmosphere of 95% air and 5% CO_2.

Cell Traversal Assays

Cell traversal events by sporozoites were visualized by spinning disk confocal microscopy. Sporozoites and freshly trypsinized cells in a 1:1 ratio were mixed to 10 μl Matrigel (BD Biosciences) in the presence of 5 μM SYTOX Orange Nucleid Acid Stain (S-11368, Molecular Probes), a high-affinity nucleic acid stain that penetrates cells with a compromised plasma membrane. Samples were recorded for 30 min in multiple z layers with a double wavelength excitation of 488 nm and 568 nm for GFP-expressing parasites and SYTOX Orange, respectively.

Cell Infection Assays and CS Staining

Infection assays were performed at a multiplicity of infection of 1. Eight-well permanox Lab-Tek chamber slides and 15 × 10^4 sporozoites freshly dissected out from mosquito salivary glands were used in experiments with rat primary hepatocytes; MatTek glass bottom culture dishes and 2 × 10^4 sporozoites were used for CRL-2017 dermal fibroblasts infection. First, sporozoites were added onto cells on ice, and samples were centrifuged for 1 min at 4°C at 800 rpm to facilitate parasite-host cell interactions. Samples were then placed at 37°C, and at various incubation times samples were fixed with 4% paraformaldehyde (PFA), which does not permeabilize the host cell plasma membrane, and stained with the 3D11 anti-CS mAb coupled to Alexa Fluor 568 (A-20184, Molecular Probes). This allowed for discriminating between internalized sporozoites (green) and external sporozoites (red). Note that, in the case of the wild-type sporozoites, a proportion of the green parasites after 1 hr correspond to sporozoites that are located inside a cell, but not inside a vacuole (sporozoites arrested during cell traversal), a proportion that does not exceed 5%–10%.

Sporozoite Attachment Assay

Infection experiments were performed with 1.75 × 10^4 salivary gland sporozoites and a confluent monolayer of CRL-2017 dermal fibroblasts plated on Lab-Tek chamber slides (8-well permanox). Sporozoites were plated on cells in the presence of cytD 1 μg/ml, and after 15 min at 37°C, samples were washed three times in PBS and then stained with an Ab-CS to differentiate intracellular from extracellular parasites. As expected, no intracellular parasites were found. In experiments with metabolic inhibited parasites, sporozoites were preincubated 1 hr at room temperature with 0.03% sodium azide and then plated on cells in the continued presence of this compound.

Transmission Electron Microscopy

Samples were fixed by addition of 2.5% glutaraldehyde/0.15 M cacodylate buffer followed by 1% osmium tetroxyde, dehydrated in a series of ethanol concentrations, and embedded in EPON resin mixture. Ultrathin sections (50 to 60 nm) were observed with a Jeol 1200EXII (Tokio, Japon) transmission electron microscope. Images were recorded using an Eloise Keenview camera and the Analysis Pro software version 3.1 (Eloise SARL, Roissy, France).

Real-Time Quantitative RT-PCR

Real-time qPCR was performed on cDNA preparations using the SYBR green detection system and the ABI Prism 7900 sequence detector (Applied Biosystems) according to the manufacturer's instructions. Salivary gland sporozoites from the ConF, SpectF, and Spect2F clones were isolated at day 21 after the blood meal. RNA was extracted with TriZol and DNase treated, and cDNAs synthesized with Superscript II reverse transcriptase (Invitrogen) using random primers. Three independent RNA preparations were made for each sample. PCR conditions were 1 cycle of 95°C for 10 min followed by 40 cycles of 95°C for 15 s, 55°C for 15 s, and 60°C for 45 min). qPCR was performed in triplicate with three serial dilutions. The standard curve was analyzed for all primers and gave amplification efficiencies of 90%–100%. Data were analyzed with SDS 2.1 software. Analysis was performed using the $2^{-\Delta\Delta Ct}$ method (User Bulletin 2, ABI). The following primers were used for qPCR analysis: Ama1, forward, ATTTGGGTTGATGGTTATTG; Ama1, reverse, TCCTTGTCGAAATTTGG TAG; CS, forward, ACAGAGGAATGGTCTCAATG; CS, reverse, TTATCCATTT TACAAATTTCAG; TRAP, forward, AACATTCACTCCATTCTTCC; TRAP, reverse, CATGTTATTCCAATGCTCAC; P36p, forward, CTAATACGACCTTAG-GACACTTTGAA; P36p, reverse, GATGTTCCATTTGGGTTTACATGATC; P36, forward, GCCTAATGCAAAATATTATCCCGATTTAG; P36, reverse, GCTAGT CCTTTGTTCCCATTATATG; Pbpl/UIS10, forward, GTTACACTGATAGAGAA GATGT; Pbpl/UIS10, reverse, GTGGTACTATACAAACAATATGTTGG; Spect2, forward, AAGGAGTTTCAGCTATGCAC; Spect2, reverse, CAGTTCATTTATG CCTGACC; Spect1, forward, TAGCCTAATTCAAATAAACGAAC; Spect1, reverse, GAAGTTAATTAATTCTGATACCCT; UIS4, forward, CCAAACCAAGCG ATCATACATACAG; UIS4, reverse, CTTCACCCACTAAATCGCTTAATTC; S6, forward, GCTAGTGAAATCGAAGAAGC; S6, reverse, GCCTTGCAAATAATG AGAAC; Hsp70, forward, TGCAGCAGATAATCAAACTC; Hsp70, reverse, ACTTCAATTTGTGGAACACC; PbActin, forward, GGAAACATTATAACAGTA GGTAATGAAAG; PbActin, reverse, GTTGTACCTCCAGATAAAACAATGTTT CC; Tsrp, forward, TAAAGATAAGAGCACGAGTTAGTAGT; Tsrp, reverse, AATTGTTACATATTTACTTAGCATTCT; Celtos, forward, GTTCTATGTTTGAG AGGCAAAAATGG; Celtos, reverse, TGATGACGAGTCTTGTTGAAATGCAC; UIS3, forward, AGTTGCAATTGCTTTGTTATCATCAGGA; UIS3, reverse, GTTCTTTATATTTTGTACTAGTGCTTGGC.

Supplemental Data

The Supplemental Data include six supplemental figures and four supplemental movies and can be found with this article online at http://www.cellhostandmicrobe.com/cgi/content/full/3/2/88/DC1/.

ACKNOWLEDGMENTS

We thank S. Shorte, P. Roux, and the other members of the "Platforme d'imagerie dynamique" (Institut Pasteur) for help with confocal microscopy; C. Bourgouin, I. Thiéry, and the other members of the "Centre de Production et d'Infection des Anophèles" (Institut Pasteur) for mosquito rearing; V. Richard from the Electron Microscopy Facility (University of Montpellier 2); G. Milon, G. Lauvau, and T. Graf for providing the *lys-gfp* mice; and Patricia Baldacci and Samantha Blazquez for comments on the manuscript. This work was supported by funds from the Institut Pasteur ("Grand Programme Horizontal Anopheles"), the Howard Hughes Medical Institute, the European Commission (FP6 BioMalPar Network of Excellence), and the Core Research for Evolutional Science and Technology (CREST). R.A. was supported by the Pasteur Institute GPH fellowship, D.G. is a BioMalPar Ph.D. student, T.I. was supported by a fellowship from the Association Pasteur-Japon, M.Y. is a CREST Scholar, and R.M. is a Howard Hughes Medical Institute International Scholar.

Received: August 2, 2007
Revised: October 18, 2007
Accepted: December 26, 2007
Published: February 13, 2008

REFERENCES

Amino, R., Martin, B., Thiberge, S., Celli, S., Shorte, S., Frischknecht, F., and Ménard, R. (2006). Quantitative imaging of *Plasmodium* transmission from mosquito to mammal. Nat. Med. *12*, 220–224.